frontiers | Frontiers in Earth Science

ORIGINAL RESEARCH
published: 09 June 2022
doi: 10.3389/feart.2022.886849

Relationship Between Nb-Ta Enrichments and Highly-Fractionated Granitic Magma Evolution in South China: Geochronological, Zircon Hf Isotopic and Geochemical Evidence From Jianfengling Granite

Chen Ze-Yi[1], *Shao Yong-Jun*[1], *Wei Han-Tao*[2] *and Wang Cheng*[3]*

[1]Key Laboratory of Metallogenic Prediction of Nonferrous Metals and Geological Environment Monitoring, Ministry of Education, School of Geosciences and Info-Physics, Central South University, Changsha, China, [2]MLR Key Laboratory of Metallogeny and Mineral Resource Assessment, Institute of Mineral Resources, Chinese Academy of Geological Sciences, Beijing, China, [3]Guangdong Provincial Key Lab of Geodynamics and Geohazards, School of Earth Sciences and Engineering, Sun Yat-sen University, Guangzhou, China

OPEN ACCESS

Edited by:
Kit Lai,
Fortescue Metals Group, Australia

Reviewed by:
Xiang Fang,
Chinese Academy of Geological Science, China
Shengchao Xue,
China University of Geosciences, China

***Correspondence:**
Wang Cheng
wangcheng6@mail.sysu.edu.cn

Specialty section:
This article was submitted to Economic Geology, a section of the journal Frontiers in Earth Science

Received: *01 March 2022*
Accepted: *16 May 2022*
Published: *09 June 2022*

Citation:
Ze-Yi C, Yong-Jun S, Han-Tao W and Cheng W (2022) Relationship Between Nb-Ta Enrichments and Highly-Fractionated Granitic Magma Evolution in South China: Geochronological, Zircon Hf Isotopic and Geochemical Evidence From Jianfengling Granite. Front. Earth Sci. 10:886849. doi: 10.3389/feart.2022.886849

The Jianfengling granite is an important ore-forming rock unit in the Xianghualing orefield in Nanling region (South China), and its magmatic evolution is vital to understand the regional niobium (Nb)-tantalum (Ta) mineralization. The Jianfengling granite comprises three gradual transitional lithofacies: porphyritic biotite monzogranite (mesophase facies), biotite monzogranite (transition facies) and topaz biotite monzogranite (central facies). All the three biotite monzogranite lithofacies are characterized by being rich in SiO_2 and Al_2O_3, poor in TFe_2O_3, CaO, MgO, TiO_2, MnO and P_2O_5, and are peraluminous high-K calc-alkaline. These rocks are remarkably enriched in Rb, Th, U, Nb and Ta, strongly depleted in Ba and Sr, and slightly depleted in Zr. The LREE/HREE decreases gradually from porphyritic biotite monzogranite, through biotite monzogranite to topaz biotite monzogranite, with increasing convex ("M-type") lanthanide tetrad effect, which similar to the highly-fractionated granite. The high Th-U ($Th_{avg.}$ = 2051.56°ppm; $U_{avg.}$ = 1,498.23°ppm, respectively) and low Th-U ($Th_{avg.}$ = 708.14°ppm; $U_{avg.}$ = 441.57°ppm, respectively) zircon grains from porphyritic biotite monzogranite yielded weighted average $^{206}Pb/^{238}U$ ages of 161.3 ± 1.6 Ma (MSWD = 1.3, *n* = 13) and 158.7 ± 2.0 Ma (MSWD = 1.7, *n* = 13), respectively, consistent with the large-scale magmatic-mineralization event in the Nanling region (ca. 160–150 Ma). The εHf(t) values of the high Th-U (-6.48 to -2.51) and low Th-U (-6.58 to -1.12) zircon grains from the porphyritic biotite monzogranite indicate that the causative magma was formed from partial melting of the Mesoproterozoic Cathaysian basement rocks in a lithospheric extension setting. The Nb and Ta contents increase with fluorine from the porphyritic to topaz biotite monzogranite, indicating that the Nb-Ta enrichment may have caused by the gradual increase of fluxing content (fluorine) during the fractionation of the Jianfengling granitic magma.

Keywords: whole-rock geochemistry, jianfengling, southern hunan, Nb-Ta mineralization, highly-differentiated granite, zircons U-Pb-Hf isotopes

INTRODUCTION

Highly-differentiated granites represent important resource of rare metals, such as Li, Be, Nb, Ta, Rb and Cs, and are also enriched in Sn, Th, Zr, U, Hf and Ga (Černý and Erict, 1985, 1992, 2005, 2012; Simmons and Webber, 2008; Thomas et al., 2011a, 2011b; Kesler et al., 2012; Linnen et al., 2012). This is because rare metals and volatiles are usually enriched in the late-stage differentiated magma (Linnen et al., 2012). In South China (**Figures 1A,B**), the W–Sn–Pb–Zn mineralization in the Nanling region possesses distinct zoning from east to west: the Shizhuyuan and Yaogangxian W deposits (east) → the Furong, Xianghualing and Furong Sn deposits (middle) → the Huangshaping and Baoshan Pb–Zn deposits (west) (**Figure 1C**). The Nanling region is also rich in rare metal resources, including Li, Be, Rb, Ta and Nb in many deposits (e.g., Jianfengling, Laiziling, Xianghualing, Tangguanpu, Changchong and Sanshiliuwan) (**Figure 1D**). The Jianfengling Nb-Ta granite and its genetic link with the Dongshan W-Sn skarn deposit represents an example of

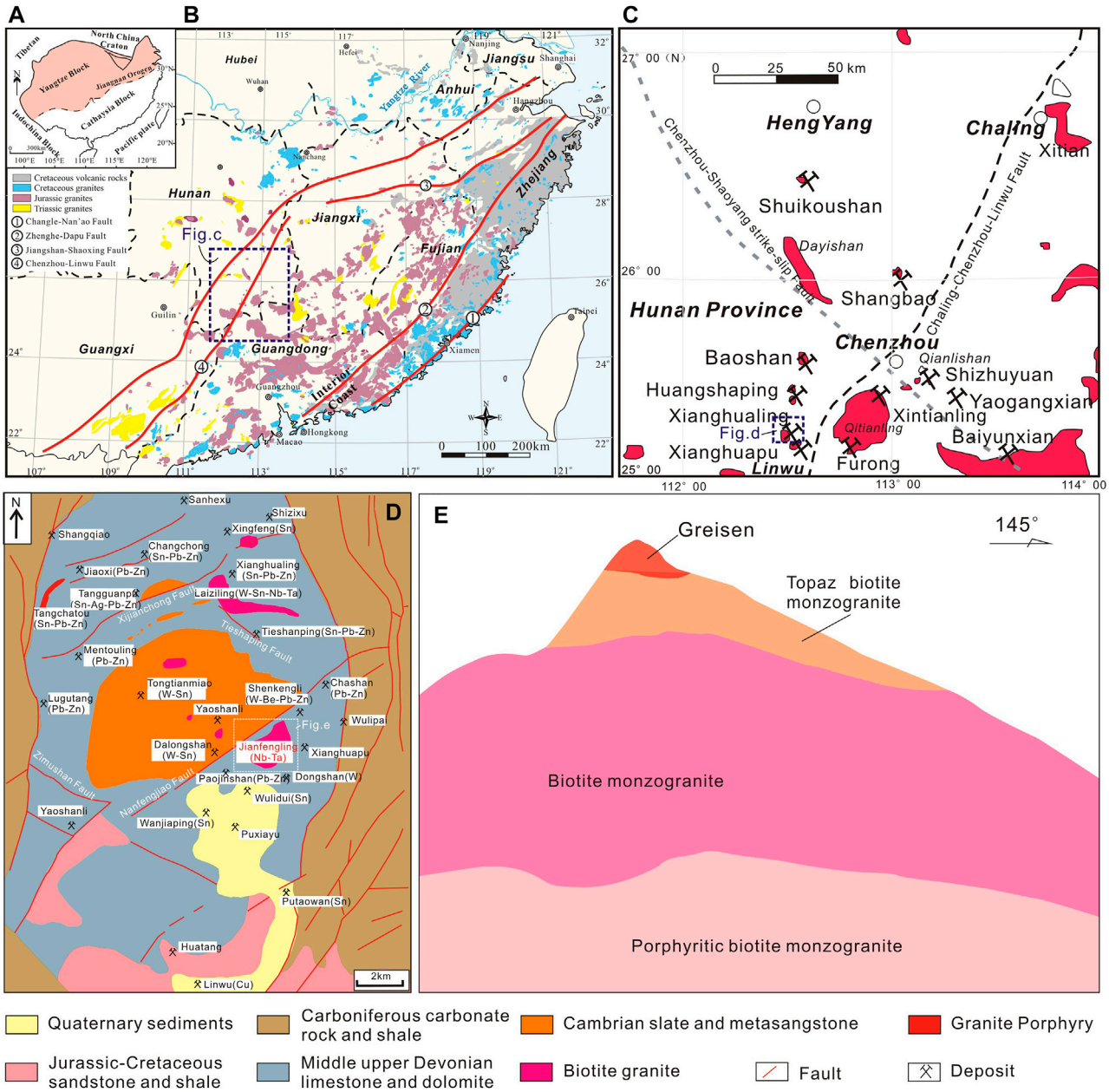

FIGURE 1 | (A,B) Map showing the Jurassic granite distribution in South China (after Wang et al., 2008). **(C)** Jurassic granites and associated W–Sn–Cu–Pb–Zn polymetallic deposits in southern Hunan (after Yao et al., 2007). Simplified geological maps of the **(D)** Xianghualing orefield (after Yang et al., 2013) and **(E)** Jianfengling granitic pluton (after Chen, 2021).

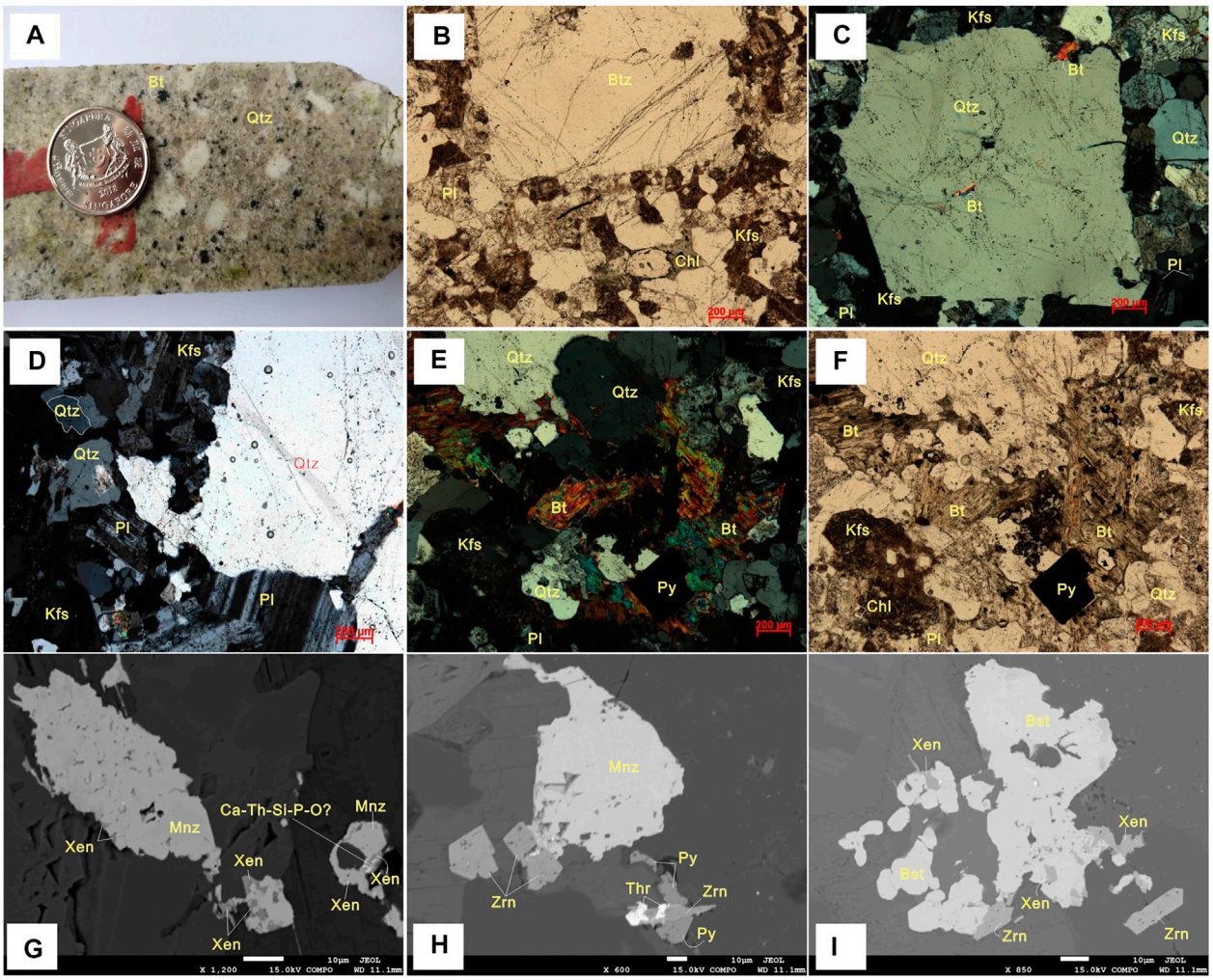

FIGURE 2 | (A) Photograph of the Jianfengling porphyritic biotite monzogranite in the field **(B–F)** Photomicrographs of porphyritic biotite monzogranite; **(G)** Monazite replaced by xenotime; **(H)** Monazite and zircon are co-junction edge structure, and zircon replaced by thorite and late pyrite; **(I)** Bastnasite replaced by xenotime and zircon. Pl, plagioclase; Kfs, K-feldspar; Qtz, quartz; Bt, biotite; Mnz, monazite; Py, pyrite; Zrn, zircon; Bst, bastnasite; Xen, xenotime; Thr, thorite.

the regional W-Sn-rare metal metallogenic system (**Figures 1D,E**; Mo, 1983, Qiu et al., 2003; Chen, 2018; 2021). The Jianfengling granite is highly-differentiated peraluminous high-K calc-alkaline. Many previous studies were focused on the age, magma source and petrogenesis (Qiu and Peng, 1997, 1998, 2002; Lai et al., 2014, 2015; Xuan et al., 2014; Wen et al., 2017; Zhu, 2020). Published zircon U-Pb ages show that the Jianfengling granite was emplaced during ca. 154.4–165.2 Ma (Xuan et al., 2014; Yang et al., 2018; Zhu, 2020). However, it is still unclear why the Jianfengling granite was emplaced over a wide age range. Besides, the K_2O and Na_2O contents of the Jianfengling granites resemble A-type (Xuan et al., 2014; Yang et al., 2018), but the low Zr saturation temperature is inconsistent with typical A-type granite formation (Chen, 2021). Furthermore, how Nb-Ta enrichments was caused by extensive granitic magma fractionation is unclear. To address these issues, we describe the geology of the Jianfengling Nb-Ta rare metal granite, and present new data on its whole-rock geochemistry and *in-situ* zircon U-Pb-Hf isotopes for the different lithofacies of the granite.

REGIONAL GEOLOGY

The Xianghualing orefield is located at the tectonic junction of the EW-trending Nanling metallogenic belt and the NE-trending Qin-Hang belt (**Figure 1B**). Since the Mesozoic, the region has undergone multiple periods of complex tectono-magmatic activities, and developed a series of granitic units and the accompanied W-Sn, Pb-Zn-Cu-Mo, and rare metal (Nb-Ta-Rb) polymetallic deposits

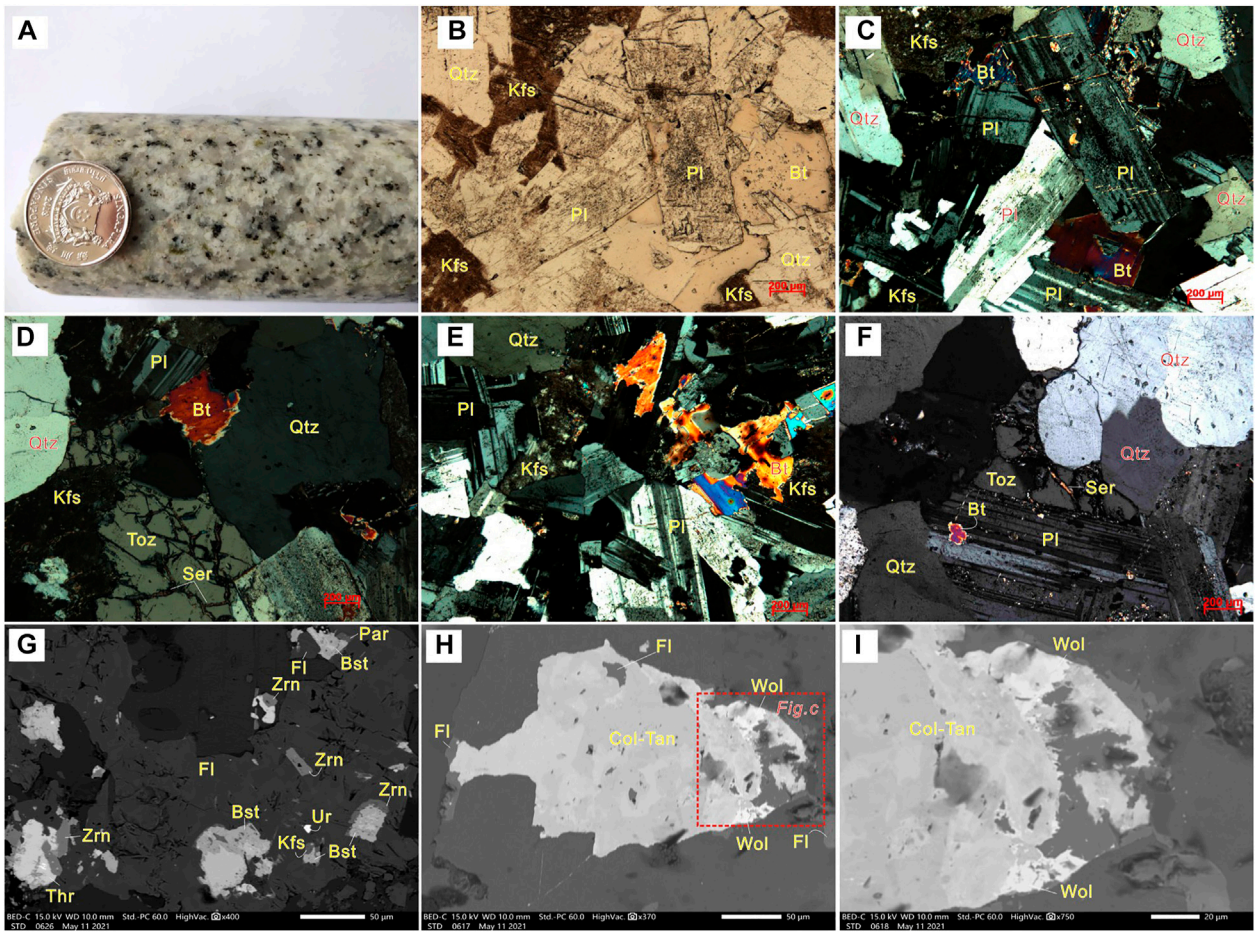

FIGURE 3 | (A) Photograph of the Jianfengling biotite monzogranite in the field **(B–F)** Photomicrographs of biotite monzogranite; **(G)** Zircon, bastnaesite, uraninite, and monazite coexist in fluorite. Bastnaesite replaced monazite, and was then replaced by zircon **(H–I)** Columbite-tantalite replaced by wolframite. Pl, plagioclase; Kfs, K-feldspar; Qtz, quartz; Bt, biotite; Toz, topaz; Mnz, monazite; Py, pyrite; Zrn, zircon; Bst, bastnasite; Xen, xenotime; Thr, thorite; Fl, fluorite; Col-tan, columbite-tantalite; Wol, wolframite.

(**Figure 1C**). The regional structure is dominated by the NS-trending Xianghualing anticline, with NS-trending reverse faults and NNE-trending closed complex linear folds on both limbs. The Tongtianmiao dome is located in the southern part of the anticlinal core. On margin of this dome, there are SW- and SE-trending conjugate tensional and strike-slip faults, NS-trending thrust faults, and NNE-trending thrust. Magmatic rocks and polymetallic mineral occurrences are distributed in/around this dome. The outcropping rocks are composed of the Cambrian to Cretaceous sequences and Quaternary sediments, among which the Devonian Xikuangshan Group and the Upper Devonian Shetianqiao Group are the main ore-host. There are over 180 (15 major) intermediate-felsic plutons in the Xianghualing orefield, covering an outcrop area of about 15 km^2 (X, 1990). Representative plutons include (from north to south) the Tongtianmiao, Yaoshan, Zanziling, Jianfengling, and Qitianling (**Figure 1C**).

JIANFENGLING GRANITE PLUTON

The Jianfengling granite pluton (outcrop area: 4.4 km^2) is located SE of Tongtianmiao anticline in the Xianghualing orefield (**Figures 1D,E**). The pluton has clear vertical/horizontal lithofacies transitional zonation:a) porphyritic biotite monzogranite (mesophase facies), b) biotite monzogranite (transition facies) and c) topaz biotite monzogranite (central facies), combined with 100 m-thick greisenization devolved on top of the Jianfengling granite (**Figure 1E**).

Fresh surface of the porphyritic biotite monzogranite is light fleshy red (**Figure 2**). The rock has massive structure, with feldspar phenocrysts of about 1–10 mm size. The samples contain mainly plagioclase (30%) and alkaline feldspar (25%), quartz (30%) and biotite (10%), as well as accessory zircon, monazite, bastnasite, thorite, xenotime, tantalite, rutile and uraninite. Alteration styles include mainly pyrite, carbonate, fluorite, silicic, argillic, and sericite.

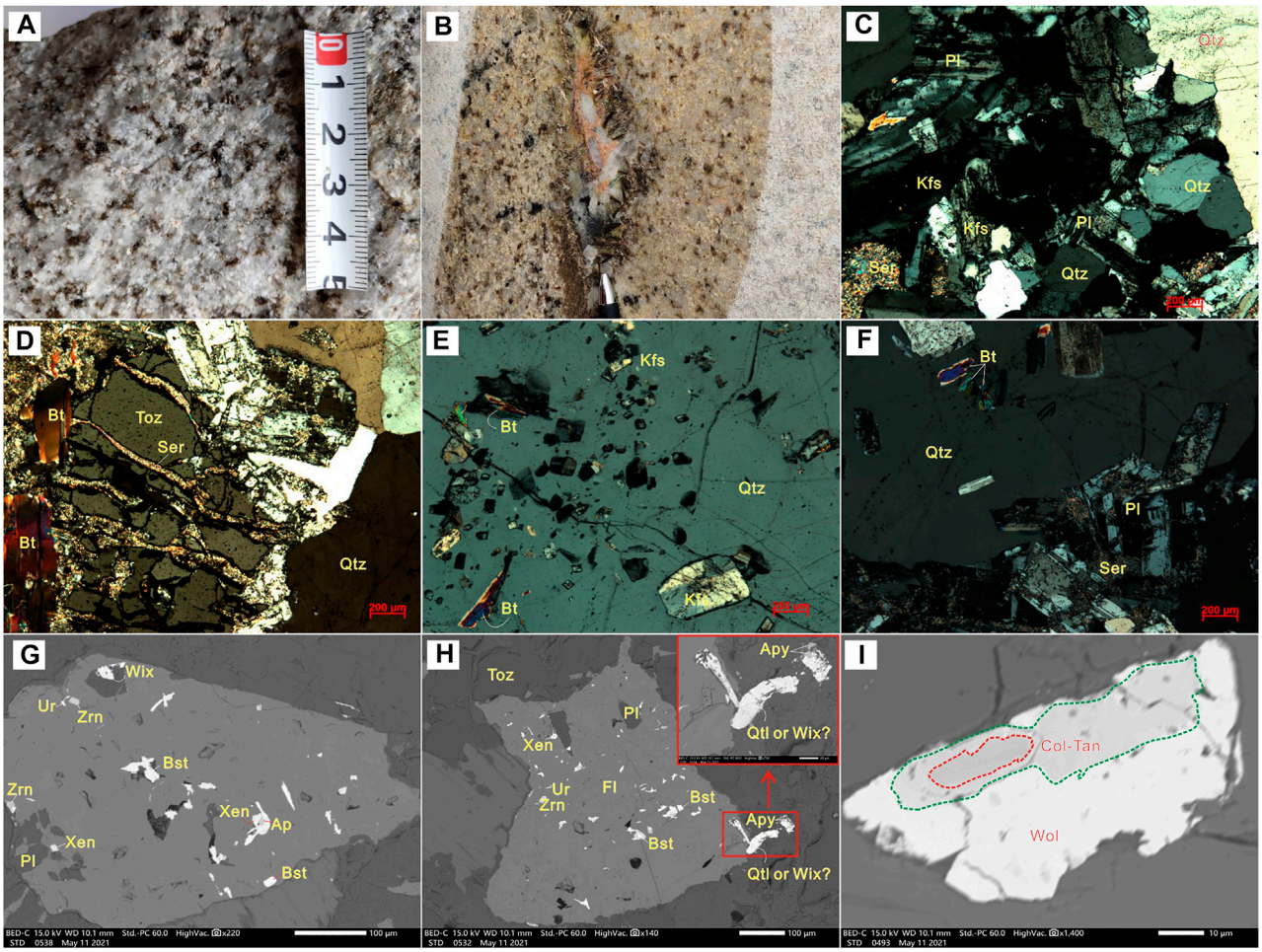

FIGURE 4 | Photographs of **(A)** topaz biotite monzogranite; **(B)** granitic pegmatite in medium-grained biotite monzogranite **(C–F)** Photomicrographs of topaz biotite monzogranite **(G–H)** Zircon, bastnaesite, uraninite, monazite, and arsenopyrite coexist within fluorite; **(I)** Multigenerational zone-banded columbite-tantalite. Pl, plagioclase; Kfs, K-feldspar; Qtz, quartz; Bt, biotite; Toz, topaz; Mnz: monazite; Py, pyrite; Zrn, zircon; Bst, bastnasite; Xen, xenotime; Thr, thorite; Fl, fluorite; Col-tan, columbite-tantalite; Wol, wolframite; Apy, arsenopyrite.

The biotite monzogranite contains mainly alkaline feldspar (25%) and plagioclase (25%), quartz (35%) and biotite (15%) (**Figure 3**). Accessory minerals are similar to its porphyritic counterpart except for the presence of topaz and fluocerite, and their alteration styles are also similar except for the absence of pyritization.

The topaz biotite monzogranite has also massive structure (**Figure 4**). The mineral composition is mainly alkaline feldspar (25%) and plagioclase (25%), quartz (30%), biotite (15%) and topaz (5%). The accessory minerals and alteration styles are both similar to its transition facies counterpart. Compared with the transition facies, the central facies has more and coarser-grained topaz. Granitic pegmatite is developed locally (**Figure 4B**), which contains mainly mica (25%), quartz (40%), K-feldspar (25%), and fluorite (10%).

ANALYTICAL TECHNIQUES

Major and trace elements geochemical analyses were undertaken at the ALS Laboratory (Guangzhou, China). Major oxide concentrations were measured with an X–ray fluorescence (XRF) spectrometer. Fused lithium borate glass disks were used, and the analytical precisions were better than ±0.01%, as estimated based on repeated analyses of the standards GSR–2 and GSR–3. The trace elements concentrations were determined by ICP–MS, using the USGS rock standards of the Columbia River 2 (BCR–2) basalt, Hawaiian Volcanic Observatory 1 (BHVO–1) basalt, and (AGV–1) andesite. The analytical precision and accuracy were better than ±5% for the trace elements studied, and the detailed analytical procedures are as described in Zhou et al. (2014).

Zircon grains were separated using standard heavy liquid and magnetic separation techniques. The selected grains were mounted in epoxy resin, polished, and gold-coated. The zircon internal texture was examined by cathodoluminescence (CL) imaging at the Sun Yat-Sen University (SYSU, Zhuhai). *In-situ* zircon U-Th-Pb dating

TABLE 1 | Whole-rock major and trace element compositions of the Jianfengling pluton.

Sample	45,302-7	45,302-8	45,302-9	45,302-10	45,302-11	45,302-12	45,302-1	45,302-2	45,302-3	45,302-4	45,302-5	45,302-6	45,004-1	45,004-2	45,004-3
	Porphyritic biotite monzogranite								Biotite monzogranite				Topaz biotite monzogranite		
SiO_2	76.67	76.11	76.68	76.08	76.29	75.93	74.56	74.19	75.78	74.78	74.65	75.32	74.77	74.99	75.88
TiO_2	0.063	0.076	0.068	0.07	0.075	0.061	0.041	0.046	0.043	0.048	0.045	0.047	0.028	0.036	0.03
Al_2O_3	12.59	12.7	12.12	12.98	12.49	12.64	13.54	13.89	13.37	13.54	13.83	13.3	13.73	13.5	13.88
TFe_2O_3	0.46	0.68	0.71	0.58	0.77	0.42	1.09	1.2	0.71	1.12	1.01	1.07	0.85	1.02	0.83
FeO	0	0	0	0	0	0	0	0	0	0	0	0	0	0	0
MnO	0.02	0.027	0.026	0.023	0.027	0.02	0.046	0.037	0.04	0.035	0.046	0.033	0.042	0.054	0.044
MgO	0.2	0.21	0.2	0.2	0.2	0.2	0.21	0.24	0.21	0.24	0.22	0.34	0.3	0.27	0.32
CaO	0.84	0.83	0.76	0.85	0.85	0.87	1.22	0.99	0.7	0.69	0.74	0.83	1.28	1.03	1.19
Na_2O	3.41	3.64	3.56	3.77	3.47	3.74	3.46	3.02	3.51	3.15	3.62	2.22	2.91	3.34	3.25
K_2O	4.97	4.52	4.46	4.86	4.68	4.87	4.43	4.83	4.81	4.73	4.38	4.69	3.53	3.48	3.44
P_2O_5	0.032	0.054	0.038	0.034	0.036	0.041	0.033	0.03	0.033	0.039	0.047	0.029	0.029	0.02	0.032
L.O.I	0.56	0.67	0.63	0.72	0.65	0.69	1.04	1.32	0.8	1.13	0.78	1.59	1.81	1.45	0.72
A/CNK	1.37	1.41	1.38	1.37	1.39	1.33	1.49	1.57	1.48	1.58	1.58	1.72	1.78	1.72	1.76
A/NK	1.5	1.56	1.51	1.5	1.53	1.47	1.72	1.77	1.61	1.72	1.73	1.92	2.13	1.98	2.07
Δ	2.09	2.01	1.91	2.25	2	2.25	1.97	1.98	2.11	1.95	2.02	1.48	1.31	1.45	1.36
AR	4.32	4.04	4.3	4.32	4.14	4.51	3.3	3.23	3.89	3.48	3.44	2.91	2.5	2.77	2.6
Rb	845	832	836	883	895	848	1,548	1,504	1,432	1,385	1,309	1,134	741	827	705
Ba	18.3	18.3	11.1	16.7	13.8	12.3	5.61	5.59	12.5	6.22	5.37	5.66	8.71	7.45	9.69
Th	26.7	47.1	38.6	42.1	41.1	31.1	30.6	13.6	33.9	25.7	28.2	11	5.06	6.72	3.4
U	28.1	34.9	36.1	35.9	34.8	33.7	40.7	24.1	40.6	31.5	33.2	22.3	9.46	18	9.2
Ta	8.21	10.8	9.74	9.72	11.6	9.98	15.2	19.5	17.9	19.1	14.8	17.9	15.8	25	20.2
Nb	48.8	62.9	57.1	54.7	65.8	54.7	81.3	80.3	86.2	90.4	74.8	86.3	46.4	75.1	55.6
Sr	12.2	14.1	12	13.6	13.3	12.8	28.9	14.3	25.1	14.9	17.1	15.1	9.58	6.58	8.13
Zr	117	138	146	128	149	117	101	120	117	115	108	110	44.4	83.3	47.4
Hf	6.37	7.79	8.59	7.47	8.39	6.9	7.01	9.09	8.52	7.94	7.49	7.79	3.03	6.87	3.45
F	5,276	4,737	4,937	5,146	5,146	4,856	11,171	9,156	6,253	7,199	8,052	7,110	8,220	7,289	6,936
Li	116	111	139	116	156	109	915	1,028	621	801	668	727	175	334	237
Y	28.9	41.1	40.7	44.2	38.3	31.4	51.4	52	36.6	46.3	38.9	39.5	23.8	26.2	16.9
La	29.5	44.8	34.9	37.7	41.2	28.6	52.7	19.3	42.9	36.4	43.6	15.9	9.13	12.6	6.46
Ce	84.8	122	97.5	102	111	82.3	135	49.1	117	89.6	112	35.8	24.9	35.5	15.8
Pr	6.93	10.7	8.52	9.04	9.96	7.03	13.1	6.42	10.7	9.04	10.6	5.07	2.99	4.28	2.16
Nd	24.2	36.5	30.1	32	34.3	25	44.5	23.8	36.7	31.2	35.8	18.7	10.6	15	7.62
Sm	6.02	8.98	7.83	8.14	8.37	6.36	11.6	7.1	9.23	8.36	9.32	5.48	3.34	4.64	2.47
Eu	0.059	0.077	0.053	0.065	0.07	0.047	0.023	0.018	0.021	0.021	0.017	0.014	0.014	0.012	0.01
Gd	5.63	8.43	7.42	7.64	7.81	6.05	11.6	7.09	9.15	8.17	8.09	5.22	2.95	4.07	2.23
Tb	1.05	1.49	1.38	1.44	1.4	1.14	2.07	1.73	1.69	1.69	1.64	1.31	0.74	0.92	0.59
Dy	6.22	8.58	8.22	8.65	8.13	6.8	12.5	12	10	10.8	9.38	9.15	5.13	6.43	4.35
Ho	1.22	1.64	1.59	1.68	1.56	1.33	2.41	2.48	1.87	2.08	1.78	1.93	1.05	1.37	0.94
Er	3.98	5.27	5.16	5.51	4.98	4.35	8.16	8.45	5.98	6.93	5.85	6.76	3.68	4.9	3.45
Tm	0.59	0.77	0.76	0.82	0.74	0.63	1.26	1.37	0.91	1.1	0.91	1.11	0.64	0.86	0.63
Yb	4.01	5.18	4.95	5.61	4.84	4.29	8.6	9.89	6.08	7.75	6.47	8.12	4.95	6.47	4.8
Lu	0.57	0.73	0.69	0.82	0.7	0.59	1.21	1.47	0.85	1.14	0.95	1.21	0.74	0.98	0.72
ΣREE	642.67	932.6	788.19	840.27	866.24	655.21	1,190.96	746.83	957.35	885.8	944.27	586.9	346.57	469.86	281.59
ΣLREE	439.57	656.4	526.74	558.48	605.38	436.59	773.1	336.96	641.17	531.33	633.28	262.9	160.16	225.54	111.8
ΣHREE	203.09	276.2	261.46	281.78	260.86	218.62	417.86	409.87	316.18	354.47	310.99	324	186.4	244.32	169.79
ΣLREE/ΣHREE	2.16	2.38	2.01	1.98	2.32	2	1.85	0.82	2.03	1.5	2.04	0.81	0.86	0.92	0.66
$(La/Yb)_N$	5.1	6	4.89	4.66	5.9	4.62	4.25	1.35	4.89	3.26	4.67	1.36	1.28	1.35	0.93

(Continued on following page)

TABLE 1 | (*Continued*) Whole-rock major and trace element compositions of the Jianfengling pluton.

Sample	45,302-7	45,302-8	45,302-9	45,302-10	45,302-11	45,302-12	45,302-1	45,302-2	45,302-3	45,302-4	45,302-5	45,302-6	45,004-1	45,004-2	45,004-3
	Porphyritic biotite monzogranite								Biotite monzogranite				Topaz biotite monzogranite		
$(La/Sm)_N$	3.07	3.12	2.79	2.9	3.08	2.81	2.84	1.7	2.91	2.72	2.93	1.81	1.71	1.7	1.64
$(Gd/Yb)_N$	1.4	1.63	1.5	1.36	1.61	1.41	1.35	0.72	1.5	1.05	1.25	0.64	0.6	0.63	0.46
δEu	0.031	0.027	0.021	0.025	0.026	0.023	0.006	0.008	0.007	0.008	0.006	0.008	0.014	0.008	0.013
δCe	1.42	1.34	1.36	1.33	1.31	1.39	1.23	1.06	1.31	1.18	1.25	0.96	1.14	1.16	1.01
$TE_{1,3}$	1.32	1.28	1.29	1.28	1.27	1.31	1.23	1.28	1.30	1.27	1.32	1.22	1.37	1.31	1.29

The lanthanide tetrad effect manifests as a split of the chondrite-normalized REE, patterns into four segments called tetrads (first tetrad La-Ce-Pr-Nd; second tetrad (Pm)-Sm-Eu-Gd; third tetrad, Gd-Tb-Dy-Ho; fourth tetrad, Er-Tm-Yb-Lu) (e.g., fidelis and siekierski, 1966; Peppard et al., 1969). The amount of the lanthanide tetrad effect (e.g., $TE_{1,3}$) in the Jianfengling granite samples was calculated with the method described by Irber (1999).

was undertaken using an iCAP-RQ-ICP-MS coupled with an ArF-193 nm GeolasHD laser-ablation system at the SYSU. A 32 μm spot size with 5 Hz laser repetition rate was used for the ablation. Zircons Plešovice (337 ± 0.4 Ma) and 91,500 (1,065 ± 5 Ma) were used as the external standards and ^{29}Si as the internal standard. Helium carrier gas was used to enhance the transport efficiency of the ablated material. Off-line raw data were processed with the GLITTER program, and the isotopic apparent and weighted mean ages were calculated with the Isoplot program (Ludwig, 2001). Zircon dates with <10% calculated discordance are considered to be valid, and $^{207}Pb/^{206}Pb$ and $^{206}Pb/^{238}U$ apparent ages were used for the older (>1 Ga) and younger (<1 Ga) zircon grains, respectively. Details of the zircon Hf isotope analytical procedures follow those given by Li et al. (2010). The 91,500 standard zircon was used for external standardization, and the resulting data were normalized to $^{176}Hf/^{177}Hf = 0.7325$. The εHf(t) values were calculated using the present-day chondrite values of $^{176}Hf/^{177}Hf = 0.282,772$ and $^{176}Lu/^{177}Hf = 0.0332$ (Blichert-Toft et al., 1997). The Hf model ages (T_{DM1}) were calculated relative to the depleted mantle, using $^{176}Hf/^{177}Hf = 0.283,250$ and $^{176}Lu/^{177}Hf = 0.0384$; whilst the two-stage Hf model ages (T_{DM2}) were calculated with the mean continental crust value of $^{176}Lu/^{177}Hf = 0.015$ (Griffin et al., 2000).

RESULTS

Whole–Rock Geochemistry

The major- and trace-element compositions of the Jianfengling granite are given in **Table 1**. Porphyritic biotite monzogranite, biotite monzogranite, and topaz biotite monzogranite have similarly high SiO_2 and Al_2O_3, but low MgO, CaO, Na_2O and K_2O contents. The samples are classified as sub-alkalic monzogranite in the QAP and SiO_2 vs ($K_2O + Na_2O$) plots (**Figures 5A,B**). The A/CNK values are above 1 (increase from porphyritic to topaz-rich lithofacies), suggesting that the rocks are peraluminous (**Figure 5C**). In addition, the rocks are K_2O-rich and fall into the high-K calc-alkaline field (**Figure 5D**).

Samples from all the three lithofacies have similar chondrite-normalized rare earth element (REE) patterns (**Figure 6A**). Porphyritic and biotite monzogranite have similar total REE content, which is higher than that of the topaz biotite monzogranite (**Table 1**). The LREE/HREE ratio decreases from the porphyritic to topaz-rich lithofacies, whereas the convex lanthanide tetrad effect ($TE_{1,3}$) increase (**Table 1** note). When normalized to primitive mantle, all the biotite monzogranite samples are enriched in Rb, Th, U, Nb, and Ta, strongly depleted in Ba and Sr, and slightly depleted in Zr (**Figure 6B**).

Zircon Trace Element Compositions and U–Pb Geochronology

From the zircon CL images, zircon grains from the porphyritic biotite granite are idiomorphic columnar (ca. 30–200 μm), with the development of oscillatory zoning (**Figures 7A–D**). Zircon grains

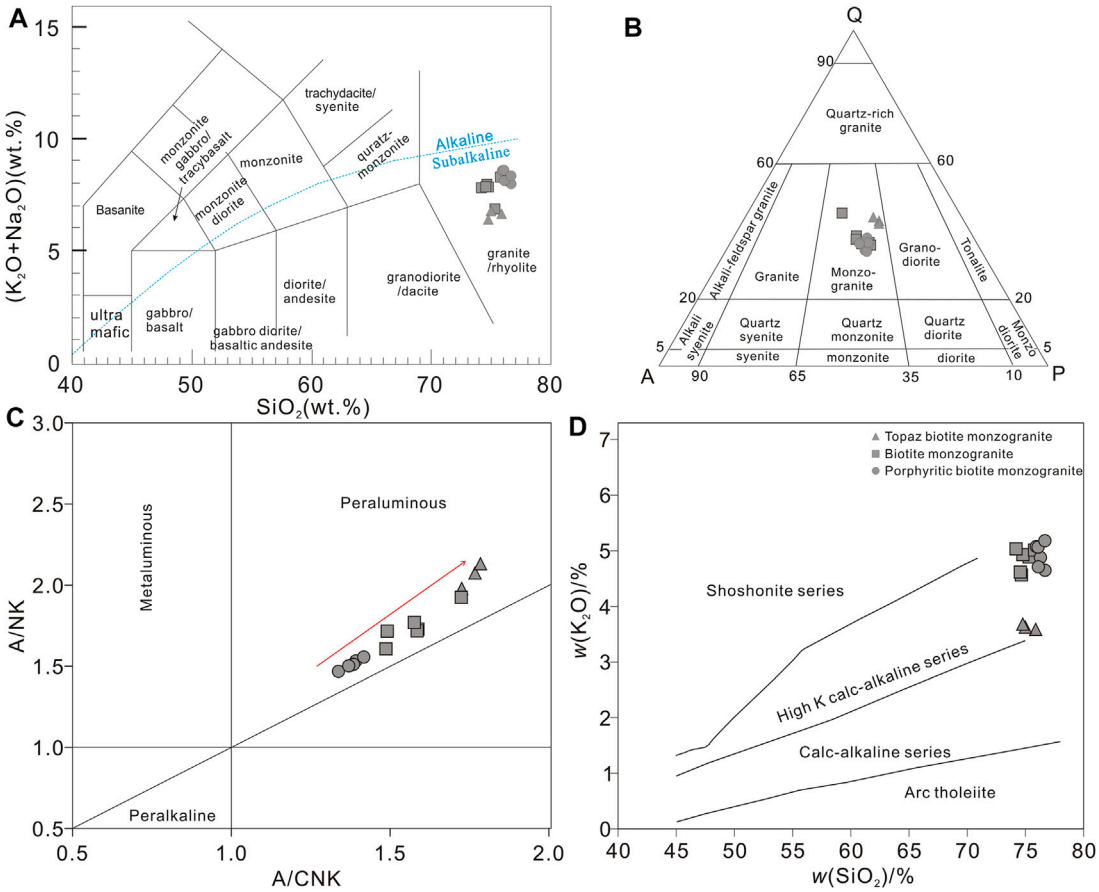

FIGURE 5 | Geochemical discrimination diagrams for the Jianfengling granitic rocks: **(A)** SiO_2 vs. (K_2O + Na_2O) (after Le Maitre, 1989); **(B)** QAP (after Streckeisen and Le Maitre, 1979); **(C)** A/KNC vs A/NK, where A/KNC = molar $Al_2O_3/(K_2O + Na_2O + CaO)$, A/NK = molar $Al_2O_3/(Na_2O + K_2O)$ (after Frost et al., 2001); **(D)** SiO_2 vs K_2O (after Le Maitre, 2002).

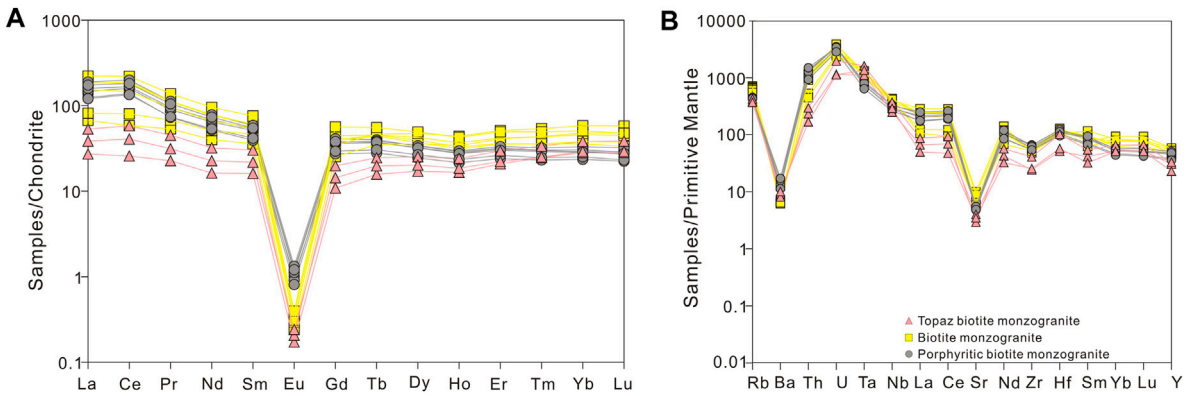

FIGURE 6 | (A) Chondrite-normalized REE patterns and **(B)** primitive mantle-normalized trace element for the Jianfengling pluton. Primitive-mantle and chondrite normalizing values are from Sun and McDonough (1989) and Taylor and McLennan (1985), respectively.

can be divided into two types, those with high CL reflectance (bright, low Th-U; **Figures 7A,B**) and low CL reflectance (dark, high Th-U; **Figures 7C,D**). Furthermore, there are irregular areas with subtle heterogeneous BSE reflectance in the grain margin of zircon from porphyritic biotite granite. Besides, thorite and pores are well-developed in these areas with heterogeneous BSE reflectance

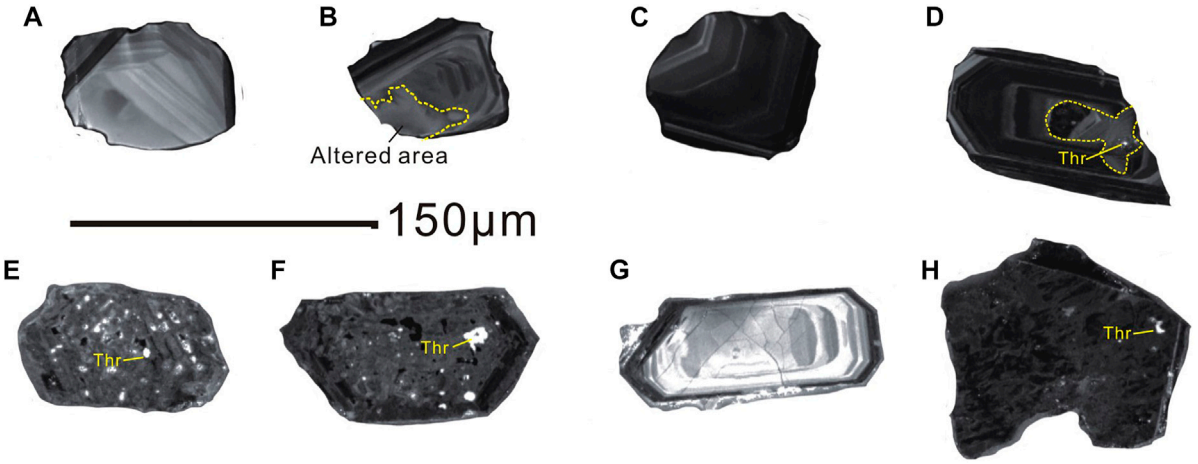

FIGURE 7 | Zircon CL images of the Jianfengling granite **(A–D)** porphyritic biotite monzogranite. Alteration is extensive on the zircon grain margin **(E,F)** medium-fine-grained biotite monzogranite **(G,H)** medium-grained biotite monzogranite. Thr, thorite.

(**Figures 7B,D**). This reflects that zircon grains were substantially fluid-modified through dissolution-reprecipitation (Putnis, 2009). In contrast, metamictization is generally developed in zircon grains from the medium-fine-grained (**Figures 7E,F**) and medium-grained (**Figures 7G,H**) lithofacies. The high Th-U zircons have Th = 454.74–4,085.56 ppm (avg. 2051.56 ppm) (**Table 2**), U = 428.76–7,404.61 ppm (avg. 2,289.82 ppm), and Th/U = 0.8–2.6 (avg. 1.50). The low Th-U zircons have Th = 279.19–1,419.34 ppm (avg. 708.14 ppm), U = 199.04–986.36 ppm (avg. 441.57 ppm), and Th/U = 1.3–2.2 (avg. 1.61). The Th and U contents and Th/U ratio in magmatic zircons are higher (Th/U > 0.5; Hoskin and Black, 2000; Belousova et al., 2002) than those of metamorphic zircons (Th/U < 0.1; Hoskin and Schaltegger, 2003). The high Th/U ratio of both types of zircons from the porphyritic lithofacies indicates a magmatic origin. In addition, chondrite-normalized REE patterns of the two types of zircons are similar to those of typical magmatic origin (**Figure 8A**). Based on the Ti-in-zircon thermometer on the porphyritic lithofacies (**Table 2**), the formation temperatures of primary magmatic- and altered high Th-U zircons are of 619–711°C (avg. 682°C) and 687–811°C (avg. 764°C) (**Figure 8B**), respectively, with the corresponding oxygen fugacity (ΔFMQ) of 0.71–7.47 (avg. 4.70) and from -12.79 to -0.27 (avg. −8.21°C) (**Figure 8C**; **Table 2**). The magmatic- and altered low Th-U zircons were estimated to have formed at 689–756°C (avg. 731°C) and 735–764°C (avg. 747°C), respectively, with their corresponding oxygen fugacity (ΔFMQ) of 1.96–6.92 (avg. 4.62) and -8.50 to -6.58°C (avg. -7.63). Thirteen high Th-U zircons yielded $^{206}Pb/^{238}U$ dates of 156.6 ± 2.4 Ma to 166.6 ± 2.3 Ma, with a weighted average of 161.3 ± 1.6 Ma (n = 13; MSWD = 1.3) (**Figure 8D**; **Table 2**). Thirteen low Th-U zircons yielded $^{206}Pb/^{238}U$ dates of 154.7 ± 2.4 Ma to 164.4 ± 2.9 Ma, with a weighted average of 158.7 ± 2.0 Ma (n = 13; MSWD = 1.7) (**Figure 8E**; **Table 2**).

Zircon Hf Isotope Compositions

The zircon Hf isotope composition data from the Jianfengling porphyritic biotite monzogranite are given in **Table 3**. The εHf(t) values of the high Th-U and low Th-U zircons are largely similar (within error), i.e., high Th-U zircon: εHf(t) = -6.48 to -2.51 (avg. -4.55), corresponding to the second-stage model age (T_{DM2}) of 1364–1613 Ma (avg. 1,492 Ma); Th-U zircon: εHf(t) = -6.58 to -1.12 (avg. -4.32), corresponding to T_{DM2} = 1,276–1,620 Ma (avg. 1,478 Ma).

DISCUSSION

Timing of Jianfengling Granite Emplacement

For the more reliable zircon U-Pb dating technique, the biotite monzogranite yielded U-Pb ages of 154.4–165.2 Ma (Xuan et al., 2014; Yang et al., 2018; Zhu, 2020). However, zircons from the biotite monzogranite are clearly metamict (**Figures 7E–H**), probably leading to the varying U-Pb dates. Zircons from the porphyritic biotite monzogranite have well-developed oscillatory zoning (**Figures 7A–D**), and fall into the dark high Th-U and light low Th-U zircon groups. Similar mineral composition (**Figures 2**–**4**) and whole–rock geochemistry (**Figures 5**, **6**) shows that the three lithofacies are products of the same magmatic evolution system, and thus the crystallization age of porphyritic biotite monzogranite (mesophase facies) can effectively represent the initial emplacement age of the Jianfengling pluton. The weighted average U-Pb age of the high Th-U zircons (161.3 ± 1.6 Ma) is consistent with that of the low Th-U zircons (158.7 ± 2.0 Ma) within error. The timing of the Jianfengling rare-metal granite emplacement is coeval with that of the Middle-Late Jurassic magmatic-metallogenic event across the Nanling region (160–150 Ma; Mao et al., 2004a, b; 2007; Li et al., 2004; Peng et al., 2006; Yuan et al., 2007; 2008; 2011; 2012a, b).

Magma Source

Zircon Hf isotopic compositions are considered to be stable during magma differentiation and hydrothermal alteration

TABLE 2 | Results of LA-ICPMS zircon U–Pb analyses for the porphyritic biotite granite from the Jianfengling pluton.

Sample	—	Th (ppm)	U (ppm)	Th/U	$^{207}Pb/^{206}Pb$	1sigma	$^{207}Pb/^{235}U$	1sigma	$^{206}Pb/^{238}U$	1sigma	$^{208}Pb/^{232}Th$	1sigma	$^{206}Pb/^{238}U$	1sigma
					Ratios		Ratios		Ratios		Ratios		age(Ma)	
302-7–25	High Th-U	2,195	1,002	2.19	0.0486	0.0014	0.1682	0.0049	0.0251	0.0004	0.0082	0.0002	160.0	2.3
302-7–32		869	505	1.72	0.0468	0.0017	0.1655	0.0060	0.0257	0.0004	0.0084	0.0002	163.4	2.5
302-7–36		1964	1907	1.03	0.0504	0.0014	0.1764	0.0050	0.0254	0.0004	0.0082	0.0002	161.6	2.4
302-7–37		1883	958	1.97	0.0478	0.0015	0.1656	0.0053	0.0251	0.0004	0.0075	0.0002	160.0	2.4
302-7–41		4,086	2,746	1.49	0.0491	0.0014	0.1664	0.0050	0.0246	0.0004	0.0076	0.0002	156.6	2.4
302-7–43		931	634	1.47	0.0495	0.0018	0.1691	0.0062	0.0248	0.0004	0.0083	0.0002	157.8	2.5
302-7–7		2,453	1,461	1.68	0.0471	0.0011	0.1699	0.0041	0.0262	0.0004	0.0083	0.0001	166.6	2.3
302-7–10		3,703	2,517	1.47	0.0478	0.0010	0.1685	0.0038	0.0256	0.0004	0.0082	0.0001	162.8	2.2
302-7–14		1893	1,452	1.30	0.0484	0.0012	0.1722	0.0043	0.0258	0.0004	0.0084	0.0002	164.4	2.3
302-7–23		1901	1,424	1.34	0.0503	0.0013	0.1743	0.0046	0.0252	0.0004	0.0083	0.0002	160.1	2.3
302-7–39		1,421	1,075	1.32	0.0485	0.0015	0.1692	0.0053	0.0253	0.0004	0.0082	0.0002	161.3	2.4
302-7–44		2,918	3,526	0.83	0.0882	0.0025	0.3072	0.0090	0.0253	0.0004	0.0251	0.0006	160.9	2.5
302-7–19		455	269	1.69	0.0577	0.0023	0.1990	0.0078	0.0251	0.0004	0.0091	0.0002	159.5	2.5
302-7–11	Low Th-U	1,419	986	1.44	0.0488	0.0013	0.1631	0.0044	0.0243	0.0003	0.0081	0.0002	154.6	2.2
302-7–17		389	254	1.53	0.0526	0.0023	0.1792	0.0076	0.0247	0.0004	0.0084	0.0002	157.4	2.5
302-7–18		480	276	1.74	0.0531	0.0022	0.1839	0.0075	0.0251	0.0004	0.0083	0.0002	160.0	2.5
302-7–20		646	377	1.72	0.0507	0.0019	0.1770	0.0065	0.0254	0.0004	0.0083	0.0002	161.5	2.5
302-7–21		865	533	1.62	0.0487	0.0016	0.1687	0.0057	0.0252	0.0004	0.0083	0.0002	160.2	2.4
302-7–24		696	399	1.74	0.0498	0.0018	0.1760	0.0065	0.0257	0.0004	0.0086	0.0002	163.4	2.5
302-7–26		531	303	1.75	0.0456	0.0019	0.1589	0.0067	0.0253	0.0004	0.0082	0.0002	161.1	2.6
302-7–29		414	270	1.53	0.0515	0.0022	0.1723	0.0075	0.0243	0.0004	0.0080	0.0002	154.6	2.5
302-7–30		878	538	1.63	0.0487	0.0017	0.1656	0.0058	0.0247	0.0004	0.0083	0.0002	157.1	2.4
302-7–31		854	512	1.67	0.0476	0.0017	0.1594	0.0058	0.0243	0.0004	0.0084	0.0002	154.7	2.4
302-7–34		595	444	1.34	0.0506	0.0019	0.1753	0.0066	0.0251	0.0004	0.0086	0.0002	159.9	2.5
302-7–40		279	199	1.40	0.0526	0.0026	0.1871	0.0093	0.0258	0.0005	0.0102	0.0003	164.4	2.9
302-7–46		1,159	649	1.79	0.0496	0.0018	0.1685	0.0063	0.0247	0.0004	0.0080	0.0002	157.1	2.5

process, and can therefore be used to reveal the origin of the magma (Kemp et al., 2007; Lenting et al., 2010). The high Th-U and low Th-U zircon grains from the Jianfengling porphyritic biotite monzogranite have similar $(^{176}Hf/^{177}Hf)_i$ (0.28249–0.28260 and 0.28249 to 0.28264, respectively) and $\varepsilon Hf(t)_{160Ma}$ values (-6.48 to -2.51 and -6.58 to -1.12, respectively) (**Table 3**), which close to the region of lower crustal evolution line (**Figure 9**). The zircon T_{DM2} ages are close to the ages (1,500 Ma) of the Proterozoic meta-sedimentary strata. This inference is further supported by the presence of Proterozoic metamorphic zircons in the granites, which represent residual zircons from the partial melting source

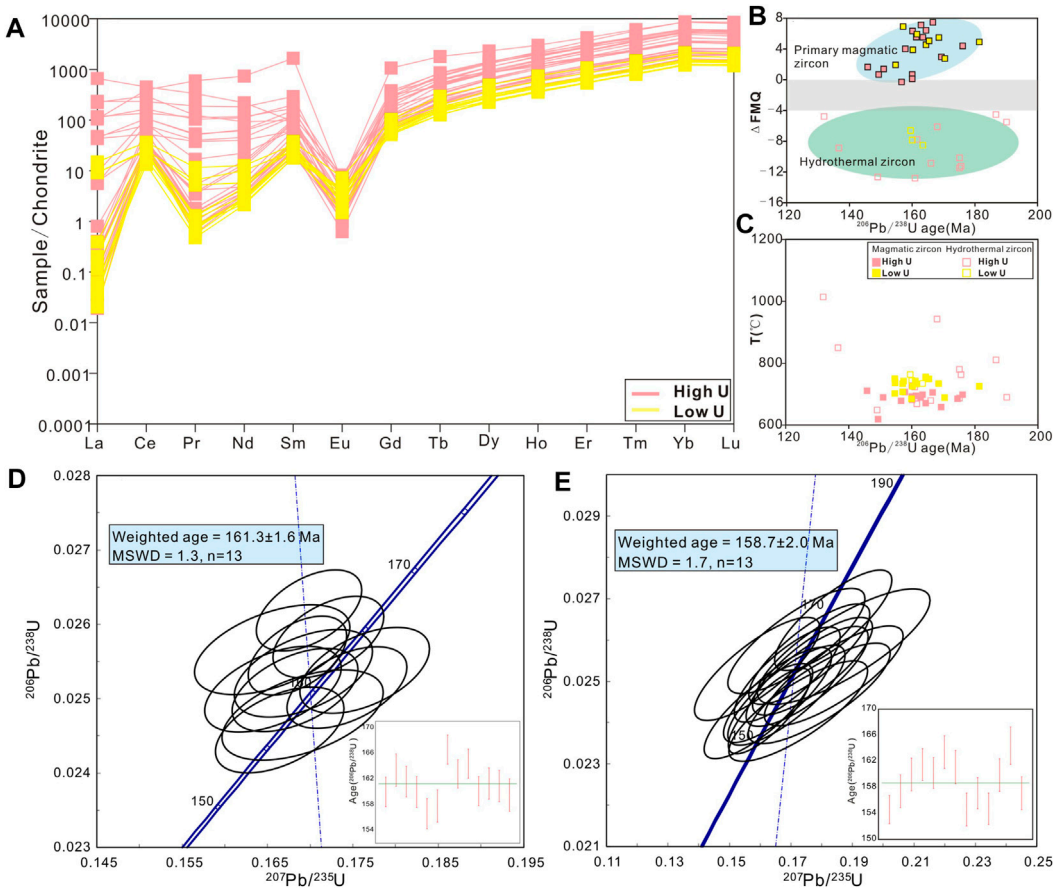

FIGURE 8 | (A) Chondrite-normalized REE patterns of different zircon groups in the Jianfengling porphyritic biotite monzogranite. Chondrite-normalized values from Taylor and McLennan (1985); **(B)** ΔFMQ vs $^{206}Pb/^{238}U$ age. Zircon oxygen fugacity was calculated from the method by Ballard et al. (2002); **(C)** Ti-in-zircon temperature vs $^{206}Pb/^{238}U$ age. The temperature was obtained with the method by Ferry and Watson (2007) **(D,E)** U–Pb concordant plots of different zircon groups in the porphyritic biotite monzogranite.

region (Li et al., 2018). Therefore, it is likely that parental magma of the Jiangfengling granite was derived from partial melting of the lower crust Proterozoic meta-sedimentary strata in South China.

Compared with the transition facies and central facies, the porphyritic lithofacies is the least fractionated (**Section 6.3**), and thus its geochemical composition is closer to the initial magma composition. The CaO/Na_2O ratio is an important index to distinguish the magma source region (Chappell and White, 1992). The CaO/Na_2O < 0.3 for the peraluminous granite formed from argillaceous rock, the CaO/Na_2O > 0.3 for the granitoid formed from psammite. The CaO/Na_2O ratio of the Jianfengling porphyritic biotite monzogranite varies in the range of 0.21–0.25, indicating that the magma was derived from the pelite rocks, such as leucogranite in Himalaya Orogen (Harris and Inger, 1992; Altherret al., 2000). In the $(CaO)/(FeO_t + MgO + TiO_2)$ vs $(CaO + FeO_t + MgO + TiO_2)$ (**Figure 10A**) and $Na_2O + K_2O + FeO_t + MgO + TiO_2$–$(Na_2O + K_2O)/(FeO_t + MgO + TiO_2)$ (**Figure 10B**), Rb/Ba–Rb/Sr (**Figure 10C**), and the Al_2O_3/TiO_2–CaO/Na_2O (**Figure 10D**) plots, the sample data points also fall into the pelite range of the clay-rich source region, indicating that the granitic magma was mainly derived from the partial melting of the meta-pelite of the crust.

Granite Petrogenesis

During the magmatic evolution, the incompatible LILEs and HFSEs would be significantly enriched in highly-fractionated magmas (Deering and Bachmann, 2010; Dostal et al., 2015; Ballouard et al., 2016). The increasing Nb, Ta, Li and Rb contents with decreasing Zr (**Figure 11**) from porphyritic biotite granite to biotite monzogranite, suggesting progressive magma fractionation (Gelman et al., 2014; Lee and Morton, 2015). However, the Nb, Li and Rb contents of the most-evolved topaz biotite monzogranite are very low, which may have been caused by the fractionation of Nb-, Li- and Rb-rich minerals, such as columbite-tantalite, lepidolite and Rb-rich biotite (**Figures 2–4**, Zhu, 2020; Chen, 2021). In the binary plots of Zr versus Zr/Hf, Nb/Ta and Y/Ho (**Figure 11**), the negative correlations from porphyritic biotite granite to topaz biotite monzogranite indicate increasing magma fractionation (Pérez-Soba and Villaseca, 2010; Ballouard et al., 2016). For

TABLE 3 | Zircon Lu-Hf results of the porphyritic biotite granite from the Jianfengling pluton.

Sample	—	$^{176}Lu/^{177}Hf_0$	$^{176}Hf/^{177}Hf_0$	$^{176}Hf/^{177}Hf_i$	εHf(t)	T_{DM} (Ma)	T_{2DM} (Ma)
302-7–1	High Th-U	0.001006	0.282,493	0.282,490	-6.47	1,074	1,613
302-7–6		0.001712	0.282,531	0.282,526	-5.20	1,040	1,533
302-7–8		0.001618	0.282,552	0.282,547	-4.44	1,007	1,485
302-7–25		0.000989	0.282,549	0.282,547	-4.46	994	1,487
302-7–33		0.000972	0.282,492	0.282,490	-6.48	1,073	1,613
302-7–37		0.001181	0.282,513	0.282,510	-5.76	1,050	1,568
302-7–7		0.001033	0.282,596	0.282,593	-2.82	929	1,383
302-7–10		0.001367	0.282,573	0.282,569	-3.67	970	1,437
302-7–12		0.001196	0.282,532	0.282,528	-5.12	1,024	1,528
302-7–14		0.000829	0.282,594	0.282,592	-2.86	927	1,386
302-7–23		0.000809	0.282,604	0.282,602	-2.51	913	1,364
302-7–39		0.000811	0.282,559	0.282,557	-4.09	975	1,463
302-7–44		0.001194	0.282,528	0.282,524	-5.25	1,030	1,536
302-7–5	Low Th-U	0.000767	0.282,541	0.282,539	-4.73	999	1,504
302-7–11		0.000964	0.282,515	0.282,512	-5.68	1,041	1,563
302-7–17		0.000619	0.282,540	0.282,538	-4.75	997	1,505
302-7–18		0.000588	0.282,598	0.282,596	-2.70	915	1,375
302-7–20		0.000618	0.282,551	0.282,549	-4.37	982	1,481
302-7–21		0.000559	0.282,520	0.282,518	-5.46	1,024	1,550
302-7–24		0.000629	0.282,599	0.282,597	-2.69	916	1,375
302-7–26		0.000569	0.282,643	0.282,641	-1.12	853	1,276
302-7–28		0.000527	0.282,573	0.282,571	-3.60	950	1,432
302-7–29		0.000515	0.282,535	0.282,534	-4.91	1,001	1,515
302-7–30		0.000676	0.282,570	0.282,568	-3.71	957	1,439
302-7–31		0.000593	0.282,503	0.282,501	-6.08	1,049	1,588
302-7–34		0.000503	0.282,488	0.282,487	-6.58	1,066	1,620
302-7–40		0.000638	0.282,597	0.282,595	-2.73	918	1,378
302-7–46		0.000624	0.282,513	0.282,511	-5.73	1,035	1,566

T = 160 Ma.

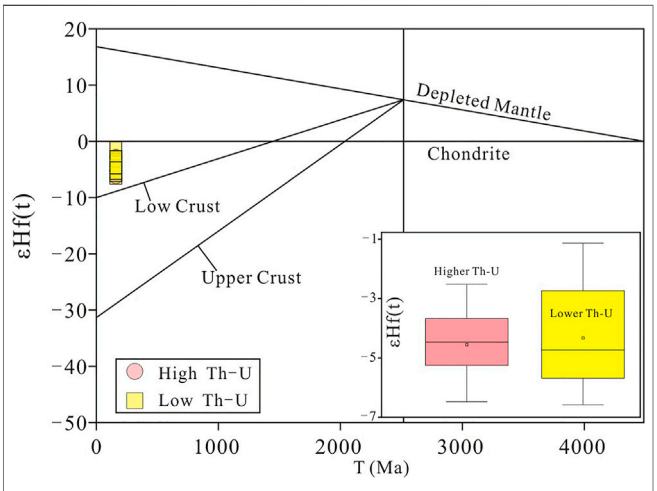

FIGURE 9 | Age vs εHf(t) plots for the Jianfengling granite samples.

granitic magma, Zr/Hf = 26 and Nb/Ta = 5 are proposed to be the boundaries between magmatic to magmatic-hydrothermal states (Bau, 1996; Ballouard et al., 2016). Except for the porphyritic biotite monzogranite, the Nb/Ta ratios of the other two lithofacies (i.e., biotite monzogranite and topaz biotite monzogranite) are all below 5, also indicating that they have experienced strong fractionation (**Figure 11**). During the fractionation of granitic magma, the total REE contents and LREE/HREE ratio would decrease significantly (Gelman et al., 2014). With the increasing Zr content, the total REE and LREE/HREE gradually decrease and the tetrad effects ($TE_{1,3}$) increase significantly (**Figure 12**).

As shown in (Zr + Ce + Y + Nb)-[(Ga/Al) ×10,000] and Zr-[(Ga/Al)×10^4] plots (**Figure 13**; Whalen et al., 1987), the porphyritic biotite monzogranite data points fall into the boundary of highly-fractionated I-, S- and A-type granites, while the biotite monzogranites and the topaz biotite monzogranites fall into the A-type granite field. However, the Zr content of the porphyritic biotite monzogranite (117–149 ppm, avg. 133 ppm), which is much lower than that of typical A-type granite (Zr ≈ 250 ppm). The (Zr + Nb + Y + Ce) content (279.5–364.1 ppm, avg. 327.2 ppm) is also below the minimum value of A-type granite (ca. 350 ppm) (Whalen et al., 1987). In addition, the temperature (from zircon Ti thermometer) for the porphyritic biotite monzogranite (619–811°C) is inconsistent with the high formation temperature of A-type granites. Although the (Ga/Al)×10,000 ratio of the porphyritic biotite monzogranite (2.52–2.72, avg. 2.64) close to the A-type granite range, the porphyritic biotite monzogranitic magma has undergone fractionation and those of highly-differentiated granites have also higher Ga/Al×10,000

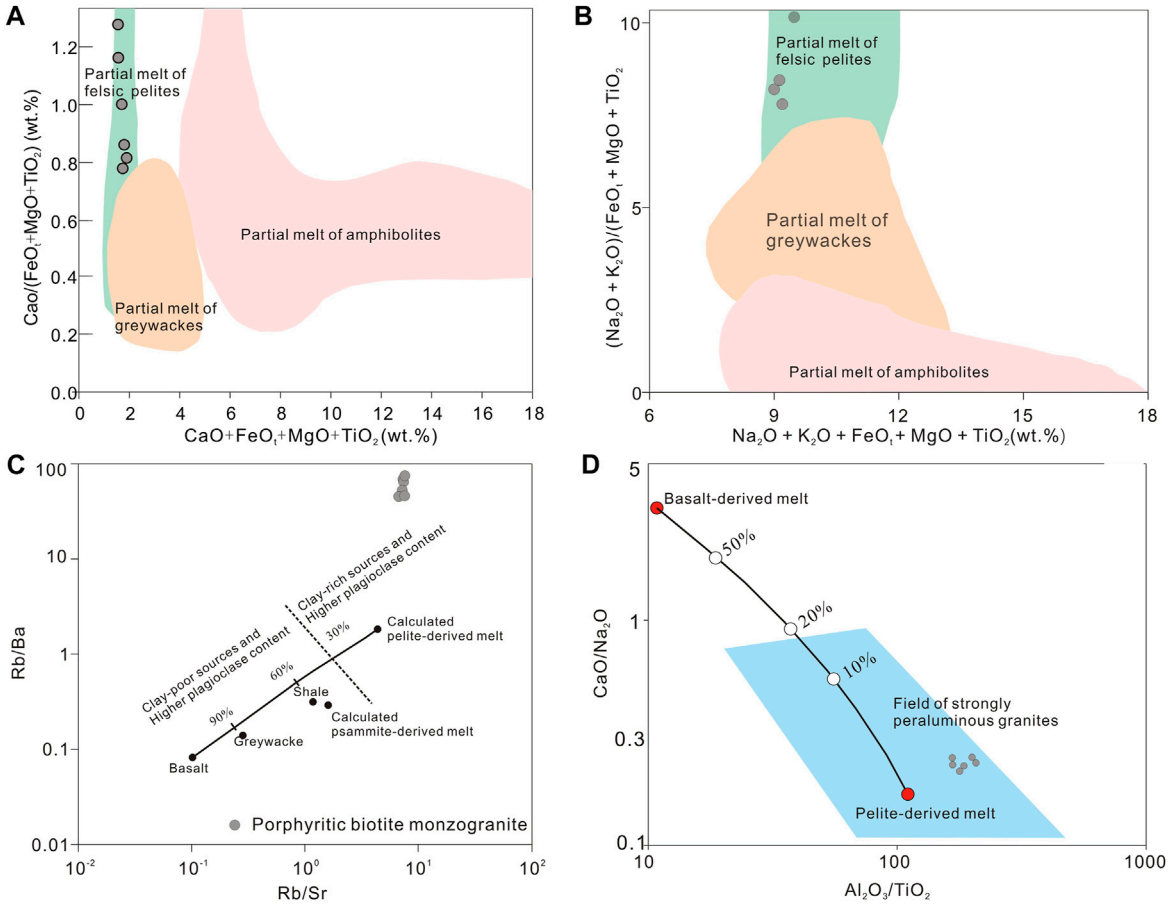

FIGURE 10 | (A) (CaO)/(FeO_t + MgO + TiO_2) vs (CaO + FeO_t + MgO + TiO_2); **(B)** (Na_2O + K_2O)/(FeO_t + MgO + TiO_2) vs (Na_2O + K_2O + FeO_t + MgO + TiO_2). Fields in **(A)** and **(B)** are from Patiño-Douce and Harris. (1999); **(C)** Rb/Ba vs Rb/Sr; **(D)** CaO/Na_2O vs Al_2O_3/TiO_2. The mixing curve between the basalt-and pelite-derived melts in **Figures 11C,D** is from Patiño-Douce and Harris (1998) and Sylvester (1998).

ratio, which is defined as A-type granites (Linnen and Cuney, 2004; Pérez-Soba and Villaseca, 2010; Breiter et al., 2013). As shown in the Zr-[(Ga/Al) × 10,000] plot (**Figure 13B**), the evolution from porphyritic to medium-fine-grained biotite monzogranite is consistent with the evolution trend of highly-differentiated I-/S-type granites. As a highly-fractionated granite, it's inevitable to be plotted in the A-type area, regardless of the Zr + Nb + Y + Ce value. A combination of FeOt/MgO (K_2O + Na_2O)/CaO and Zr + Nd + Y + Ce value is a proper parameter to discuss the highly-fractionated granite (Whalen et al., 1987). In the diagrams of FeO_t/MgO vs Zr + Nd + Y + Ce (**Figure 13C**), and (K_2O + Na_2O)/CaO vs Zr + Nd + Y + Ce (**Figure 13D**), these granites have lower FeO_t/MgO and (K_2O + Na_2O)/CaO than that of typical A-type granite. Some granite sample points do not fall into the high fractionated granite region, however, this does not mean that these are not highly fractionated granites, probably because of biotite (resulting in significantly lower K_2O and FeO_t content) and columbite-tantalite (resulting in a significant reduction in FeO_t contents). In addition, petrography, whole-rocks geochemistry, and REE tetrad effect (>1.1; eg., Irber, 1999) all indicate that these granites are highly fractionated granites. Furthermore, with decreasing Zr content, the P_2O_5, Rb and Th evolution trends (gradually decrease) of the Jianfengling granite are similar to those of highly-differentiated S-type granites (e.g., Chappell and White, 1992; Li et al., 2007, **Figures 13E,F**).

Tectonic Settings

The Early Jurassic (205–180 Ma) marked a relatively calm period for the tectonism and magmatism in South China (Zhou et al., 2006). Maruyama and Seno (1986) and Wan and Zhu (2002) suggested that the Paleo-Pacific block began to move NW and subducted at a low angle beneath Eurasia in the Jurassic. Mao et al. (2011) also inferred that the Paleo-Pacific block subducted NW at a low angle beneath the Eurasia block at ~175 Ma. Due to the NW-dipping Paleo-Pacific subduction, the eastern continental margin of China became an active continental margin, and remelting of the subducting plate occurred along the Qin–Hang paleo-suture zone and Nanling region. Meanwhile, the continental crust may have continued to thicken, and a series of crustal-scale extensional faults were developed in the backarc region (Mao et al., 2011; Wang et al., 2018). The development of bimodal magmatism (158–179 Ma; Chen et al., 2002), A-type

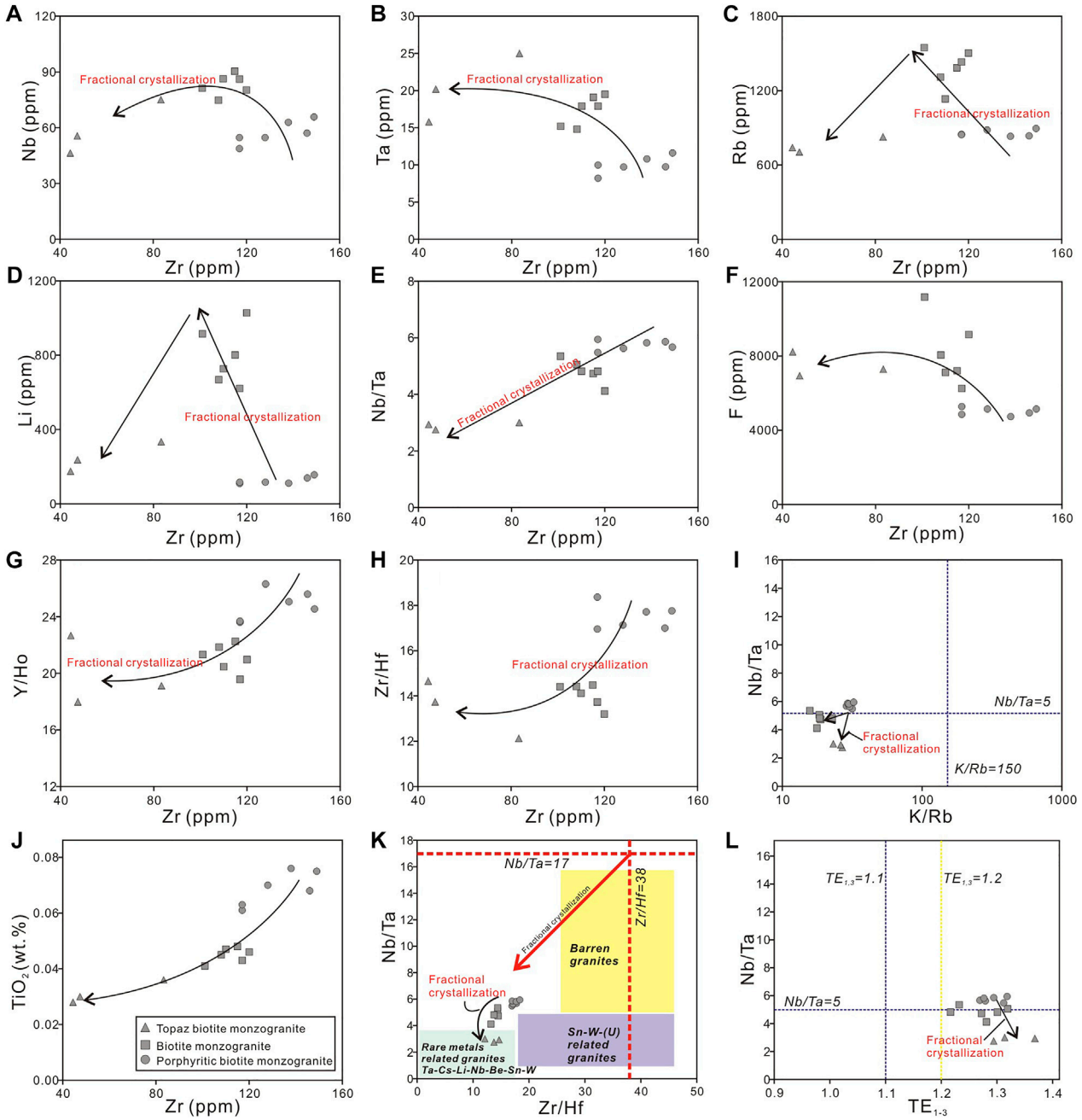

FIGURE 11 | Plots of Zr vs **(A)** Nb, **(B)** Ta, **(C)** Rb, **(D)** Li, **(E)** Nb/Ta, **(F)** F, **(G)** Y/Ho, **(H)** Zr/Hf, and **(I)** Nb/Ta vs K/Rb **(J)** Zr vs TiO_2 **(K)** Nb/Ta vs Zr/Hf **(L)** Nb/Ta vs $TE_{1,3}$ for the different Jianfengling biotite monzogranite lithofacies.

granite and alkaline plutons (165–173 Ma; Li et al., 2003), and the low–t_{DM} and high–εNd granite belt that extends from Hangzhou through Jiangxi and Hunan to Shiwandashan (**Figure 1** in Gilder et al., 1996) all demonstrate that the northeastern Qin–Hang metallogenic belt was under extension in the Middle Jurassic (Gilder et al., 1996). The South China crust may have been extended and thinned in the Mesozoic (Xu, 2012; Wang et al., 2012; Mao et al., 2013; Wang et al., 2017), triggering mantle upwelling and underplating of mantle-derived materials along fractures in the extended continental margin (**Figures 14A,B**). In summary, the ca. 172–145 Ma Nanling granites in the Qin–Hang belt were likely developed in a backarc extensional setting related to the low-angle Paleo-Pacific subduction (Jiang et al., 2006; Mao et al., 2011). In the Y vs Nb and Yb vs Ta plots (**Figures 14C,D**; after Pearce, 1996), the Jianfengling granite sample points both fell into the area of the within-plate granite, also indicating that the magma was formed through lithosphere thinning.

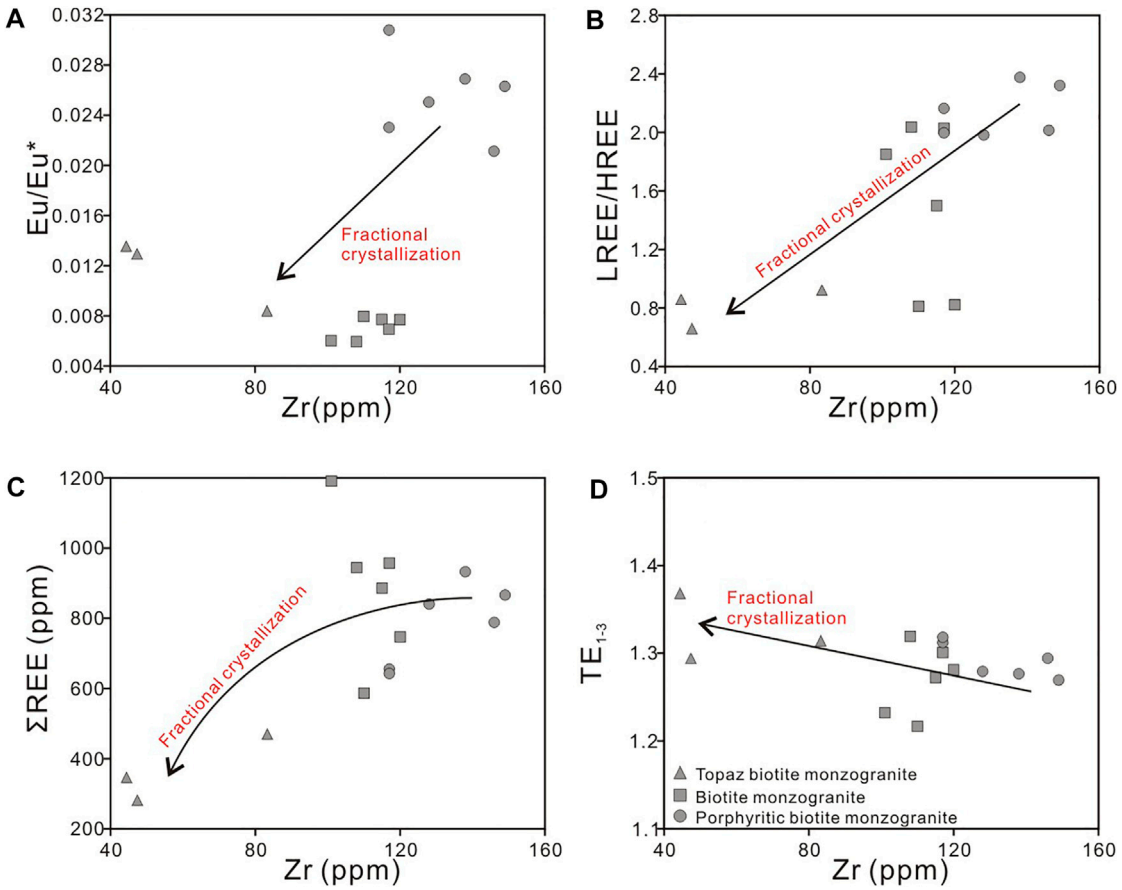

FIGURE 12 | Plots of Zr vs **(A)** Eu/Eu*, **(B)** LREE/HREE, **(C)** ∑REE, and **(D)** $TE_{1,3}$ for the different biotite monzogranite lithofacies from the Jianfengling pluton.

Magma Fractionation and Nb-Ta Enrichments

The Rb-Sr and Ba-Sr plots (**Figures 15A,B**) show fractionation of K-feldspar and plagioclase, consistent with the strong Eu/Eu* depletions of the Jianfengling granite. Granitic magmatic-hydrothermal evolution comprises generally two stages: 1) granite gradually evolved into highly-differentiated pegmatite (Trumbull and Chaussidon, 1999); 2) from granitic magma to magmatic-hydrothermal fluid, which is characterized by widespread greisenization and quartz veins (Roda-Robles et al., 2012; Pirajno, 2013; Breiter et al., 2017, 2019). Pegmatite, greisenization and W-Sn mineralization are developed in the Jianfengling biotite monzogranite, indicating that both stages are present in the evolution of the Jianfengling granitic magma. Compared with the porphyritic biotite monzogranite, tantalum content in the biotite monzogranites and the topaz biotite monzogranites increases significantly, whereas the Nb/Ta ratio decreases (**Figures 11B–E**). The TiO_2 content decreases with increasing Zr, indicating the fractionation of Ti-rich minerals (**Figure 11J**). Biotite is a Ti-rich mineral and their crystallization is conducive to Ta enrichment in the granitic magma (Stepanov and Hermann, 2013; Stepanov et al., 2014). Biotite fractionation would also increase the magma Nb/Ta ratio (Stepanov and Hermann, 2013; Stepanov et al., 2014), however, which is not found in our samples. The compatibility of Nb and Ta in granitic melt depends on the activity of non-bridging oxygen (NBOs) (Van Lichtervelde et al., 2011). The ratio $^{rt/melt}D_{Nb}/D_{Ta}$ is 0.8–1.0 for more silicic melts, remaining <1 for all examined silicate melts (Schmidta et al., 2004). The fractional crystallization of rutile would lead to a significant increase in melt Nb/Ta, contrary to our observations (i.e., **Figure 11E**). Amphibole-rich melts have been proposed to be one such candidate due to the preferential partitioning of Nb over Ta into amphibole, and which, however, is not found in our samples (i.e., **Figures 15A,B**). Moreover, Niobium (Nb), tantalum (Ta), zirconium (Zr) and hafnium (Hf) are moderately incompatible to weakly compatible (Hf at low temperature), with the exception of titanium, which is compatible in the amphibole structure (Nandedkar et al., 2016). Partition coefficient ratios $^{Amph/L}D_{Nb}/^{Amph/L}D_{Ta}$ (0.89–1.41) and $^{Amph/L}D_{Zr}/^{Amph/L}D_{Hf}$ (0.44–0.75) generally

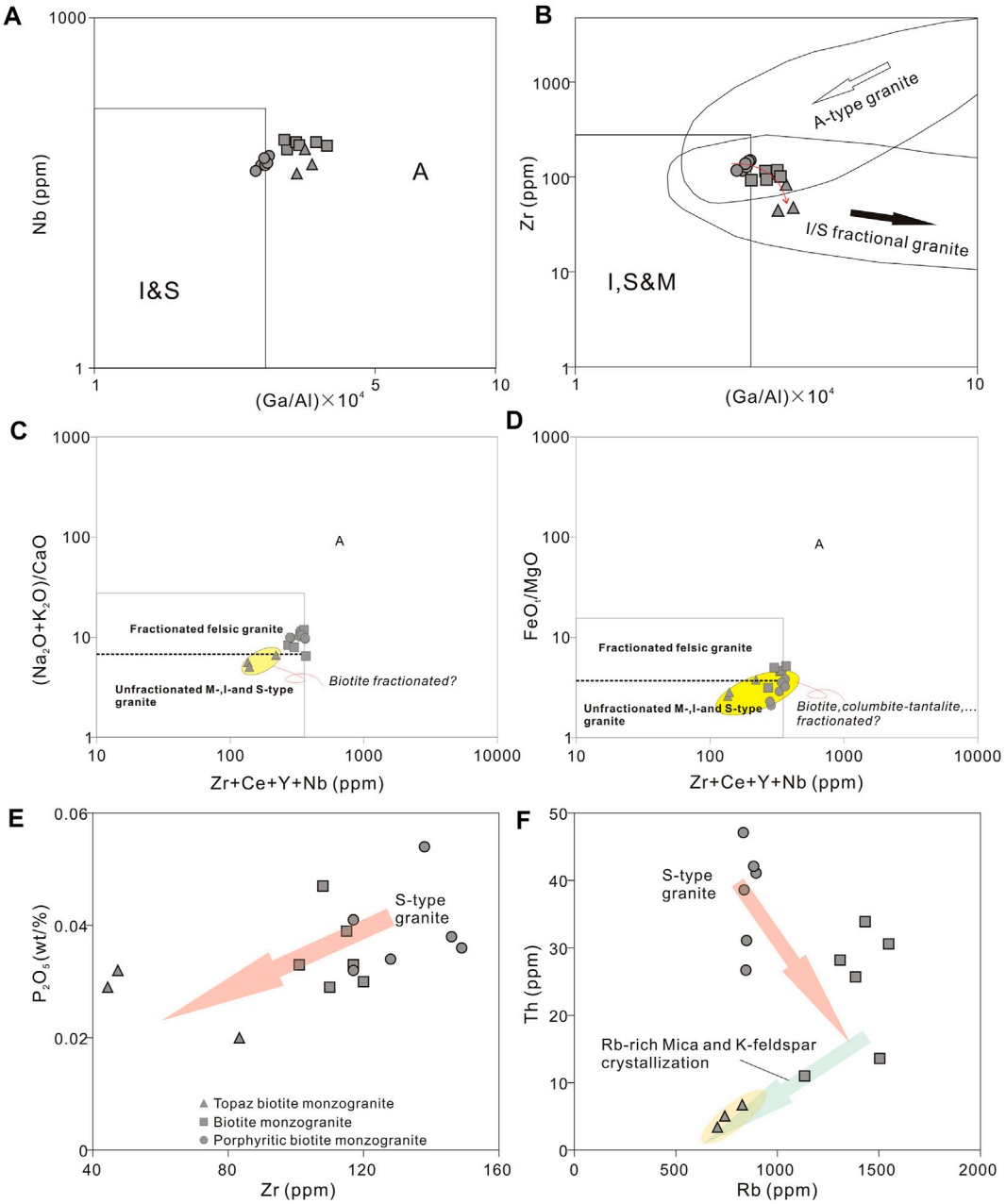

FIGURE 13 | (A) Nb vs (Ga/Al)×10^4; **(B)** Zr vs (Ga/Al) ×10^4; **(C)** (Na_2O + K_2O)/(CaO) vs (Zr + Ce + Y + Nb); **(D)** FeO_t/MgO vs (Zr + Ce + Y + Nb). **(A)**, **(B)**, **(C)** and **(D)** after Whalen et al. (1987) and Wu et al. (2017), respectively; **(E)** P_2O_5 vs Zr; **(F)** Th vs Rb for the different biotite monzogranite lithofacies from the Jianfengling pluton.

increase with decreasing temperature but no systematic trends are evident for the case of Zr and Hf, indicating that other factors are controlling the partition coefficient ratios (Nandedkar et al., 2016). Thus, the fractional crystallization of amphibole would lead to a significant increase in melt Zr/Hf, contrary to our observations (i.e., **Figure 11H**). Fluorine (F) can generally replace O in tetrahedral complex anion $[AlO_2]^-$ in the granitic melt, resulting in the decoupling of $[AlO_2]^-$. Meanwhile, fluorine would complex with Al to form AlF_6^{3-} complex [$3(Na,K)AlSi_3O_8 + 6F - 3O \rightleftharpoons (Na,K)_3AlF_6 + Al_2O_3 + 9SiO_2$; Keppler, 1993], which can significantly increase the magma non-bridging oxygen (NBOs) content. This could neutralize the excess alkali metal ions (Na^+ and K^+), and thus increase the Nb-Ta solubility in the melt (Keppler, 1993; Mysen, 1990). With magma fractionation (**section 6.3**), the contents of F, Nb and Ta in the Jianfengling granitic magma increase gradually (**Figures 15C,D**). This indicates that the F-rich volatile enrichment can significantly

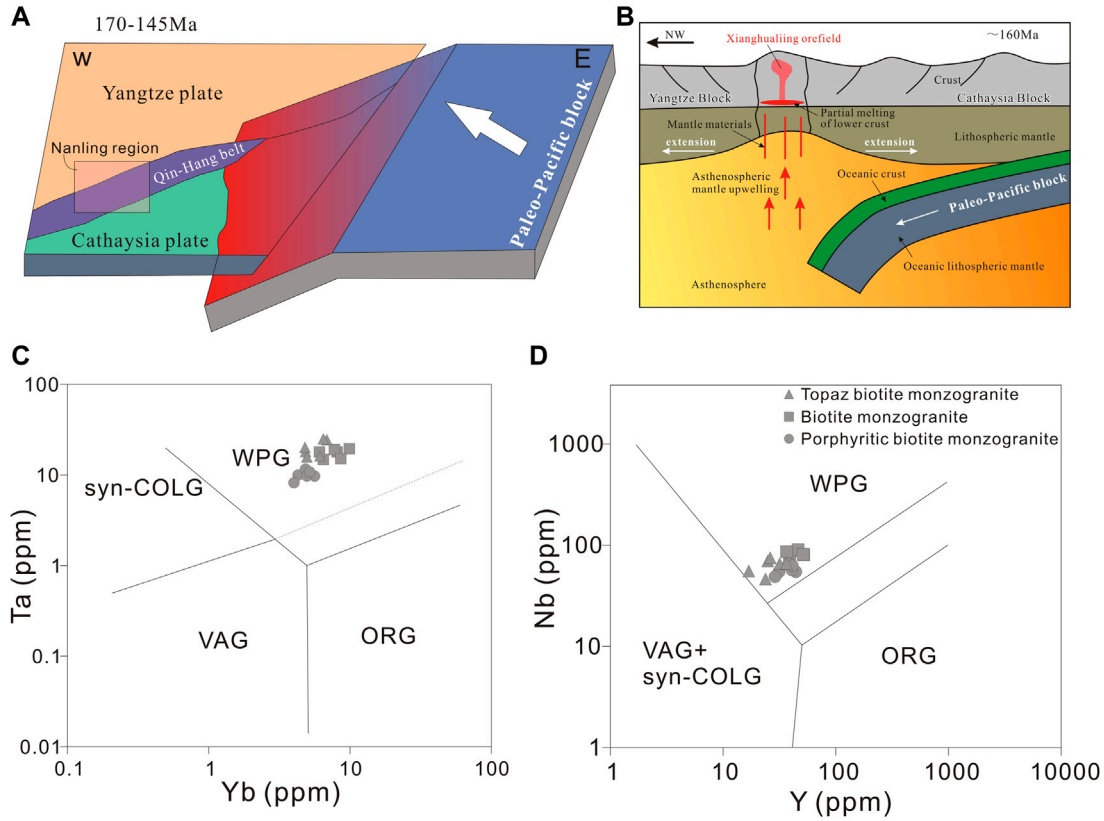

FIGURE 14 | Sketch diagram of the deep dynamic evolution of the Mesozoic metallogenesis of the Xianghualing orefield **(A,B)**. Discrimination diagrams of granite type and tectonic setting for the Jianfengling granitic rocks: **(C)** Y vs Nb; and **(D)** Yb vs Ta. Base maps after Pearce (1996).

increase the Nb-Ta solubility in the melt (Mysen and RyersonVirgo, 1981; London et al., 1993; Xiong et al., 1999).

CONCLUSION

1) The Jianfengling biotite monzogranite pluton comprises three gradual transitional lithofacies: porphyritic (mesophase facies), the biotite monzogranites (transition facies) and the topaz biotite monzogranites (central facies).
2) The high Th-U and low Th-U zircon grains from porphyritic biotite monzogranite yielded weighted average $^{206}Pb/^{238}U$ ages of 161.3 ± 1.6 and 158.7 ± 2.0 Ma, respectively, coeval with the timing of large-scale magmatism-mineralization in the Nanling region (ca. 160–150 Ma). The εHf(t) values of the high Th-U zircons (-6.48 to -2.51) and low Th-U zircons (-6.58 to -1.12) from the porphyritic biotite monzogranite indicate that the parental magma was mainly derived from partial melting of Mesoproterozoic Cathaysian basement rocks under lithospheric extension.
3) The Nb and Ta contents increase with fluorine along with magma fractionation, indicating that the Nb-Ta enrichments was likely resulted from the gradual increase of fluxing content (fluorine) during extensive fractional crystallization of the Jianfengling granitic magma.

DATA AVAILABILITY STATEMENT

The original contributions presented in the study are included in the article/Supplementary Material, further inquiries can be directed to the corresponding author.

AUTHOR CONTRIBUTIONS

CZ-Y, WH-T and W-C conceived this research. CZ-Y wrotes the manuscript and prepares the figures. SY-J and WC reviews and supervises the manuscript. The co-authors XD are involved in the discussion of the manuscript. All authors finally approved the manuscript and thus agreed to be accountable for this work.

FUNDING

This research was supported by the Fundamental Research Funds for the Central Universities, Sun Yat-sen University (2021qntd23) and the Fundamental Research Funds for the Central Universities, Sun Yat-sen University (22qntd2101). This research was supported by the Innovation-driven Plan of Central South University (2018zzts196), National Natural Science

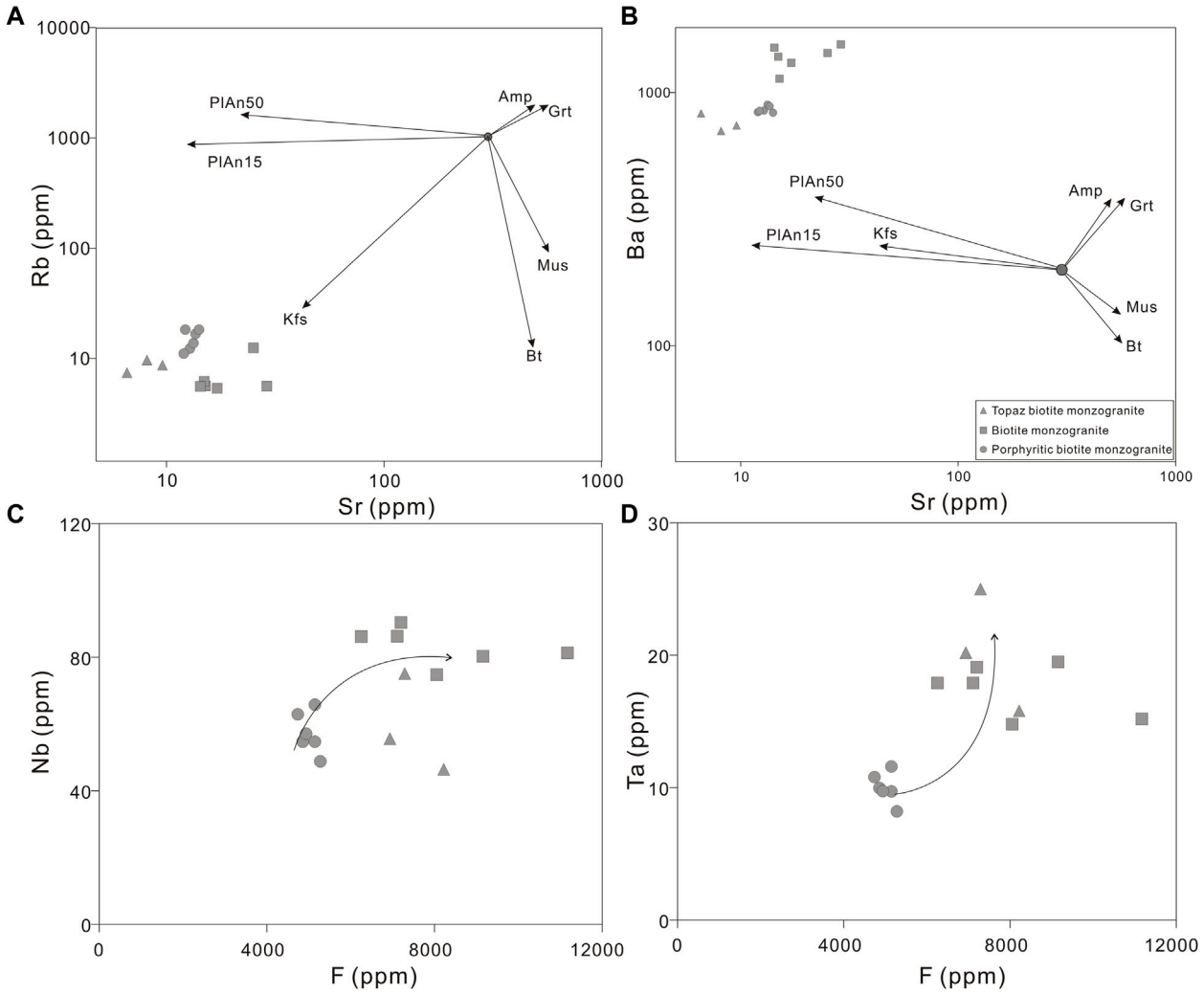

FIGURE 15 | Plots of **(A)** Rb vs Sr; **(B)** Ba vs Sr; **(C)** Nb vs F; **(D)** Ta vs F for the different biotite monzogranite lithofacies from the Jianfengling pluton.

Foundation of China (41702078), Hunan Provincial Geoscientific Research of Land and Resources (2016-04), and General Financial Grant from the China Postdoctoral Science Foundation (2017M622596).

ACKNOWLEDGMENTS

We are grateful to the #416 Brigade of the Hunan BGMR for the field assistance.

REFERENCES

Altherr, R., Holl, A., Hegner, E., Langer, C., and Kreuzer, H. (2000). High-potassium, Calc-Alkaline I-type Plutonism in the European Variscides: Northern Vosges (France) and Northern Schwarzwald (Germany). *Lithos* 50, 51–73. doi:10.1016/s0024-4937(99)00052-3

Ballard, J. R., Palin, M. J., and Campbell, I. H. (2002). Relative Oxidation States of Magmas Inferred from Ce(IV)/Ce(III) in Zircon: Application to Porphyry Copper Deposits of Northern Chile. *Contrib. Mineral. Pet.* 144, 347–364. doi:10.1007/s00410-002-0402-5

Ballouard, C., Poujol, M., Boulvais, P., Branquet, Y., Tartèse, R., and Vigneresse, J.-L. (2016). Nb-Ta Fractionation in Peraluminous Granites: A Marker of the Magmatic-Hydrothermal Transition. *Geology* 44, 231–234. doi:10.1130/g37475.1

Bau, M. (1996). Controls on the Fractionation of Isovalent Trace Elements in Magmatic and Aqueous Systems: Evidence from Y/Ho, Zr/Hf, and Lanthanide Tetrad Effect. *Contributions Mineralogy Petrology* 123, 323–333. doi:10.1007/s004100050159

Belousova, E., Griffin, W., O'Reilly, S. Y., and Fisher, N. (2002). Igneous Zircon: Trace Element Composition as an Indicator of Source Rock Type. *Contrib. Mineral. Pet.* 143, 602–622. doi:10.1007/s00410-002-0364-7

Blichert-Toft, J., Chauvel, C., and Albarède, F. (1997). Separation of Hf and Lu for High-Precision Isotope Analysis of Rock Samples by Magnetic Sector-Multiple Collector ICP-MS. *Contributions Mineralogy Petrology* 127 (3), 248–260. doi:10.1007/s004100050278

Breiter, K., Ďurišová, J., Hrstka, T., Korbelová, Z., Hložková Vaňková, M., Vašinová Galiová, M., et al. (2017). Assessment of Magmatic vs. Metasomatic Processes in Rare-Metal Granites: A Case Study of the Cínovec/Zinnwald Sn-W-Li Deposit, Central Europe. *Lithos* 292-293, 198–217. doi:10.1016/j.lithos.2017.08.015

Breiter, K., Gardenová, N., Kanický, V., and Vaculovič, T. (2013). Gallium and Germanium Geochemistry during Magmatic Fractionation and Post-magmatic Alteration in Different Types of Granitoids: A Case Study from the Bohemian Massif (Czech Republic). *Geol. Carpathica* 64, 171–180b. doi:10.2478/geoca-2013-0018

Breiter, K., Hložková, M., Korbelová, Z., and Galiová, M. V. (2019). Diversity of Lithium Mica Compositions in Mineralized Granite-Greisen System: Cínovec Li-Sn-W Deposit, Erzgebirge. *Ore Geol. Rev.* 106, 12–27. doi:10.1016/j.oregeorev.2019.01.013

Černý, P., and Ercit, T. S. (1985). Some Recent Advances in the Mineralogy and Geochemistry of Nb and Ta in Rare-Element Granitic Pegmatites. *Bull. De. Mineral.* 108, 499. doi:10.3406/bulmi.1985.7846

Černý, P., and Ercit, T. S. (2005). The Classification of Granitic Pegmatites Revisited. *Can. Mineralogist* 43, 2005. doi:10.2113/gscanmin.43.6.2005

Černý, P., Novak, M., and Chapman, R. (1992). Effects of Sillimanite-Grade Metamorphism and Shearing on Nb-Ta Oxide Minerals in Granitic Pegmatites, Marsikov, Northern Moravia, Czechoslovakia. *Can. Mineral.* 30, 699

Černý, P., Corkery, M. T., Halden, N. M., Ferreira, K., Brisbin, W. C., Chackowsky, L. E., and Meintzer, R. E. (2012). Extreme Fractionation and Deformation of the Leucogranite – Pegmatite Suite at Red Cross Lake, Manitoba, canada. Ii. Petrology of the Leucogranites and Pegmatites. *Can. Mineral.* 50, 1793–1806. doi:10.3749/canmin.50.6.1793

Chappell, B. W., and White, A. J. R. (1992). I- and S-type Granites in the Lachlan Fold Belt. *Earth Environ. Sci. Trans. R. Soc. Edinb.* 83, 1–26. doi:10.1017/s0263593300007720

Chen, P., Hua, R., Zhang, B., Lu, J., and Fan, C. (2002). Early Yanshanian Post-orogenic Granitoids in the Nanling Region. *Sci. China Ser. D-Earth Sci.* 45 (8), 755–768. (in Chinese). doi:10.1007/bf02878432

Chen, Z. Y. (2018). Ore-controlling Structure Characteristics and Prospecting Potential of Dongshan Tungsten Deposit. *Mineral Resour. Geol.* 32 (02), 222–226. (in Chinese).

Chen, Z. Y. (2021). *Rock- and Ore-Forming Mechanism of the Jianfengling Rb-Nb-Ta Deposit in Xianghualing Orefield, Hunan Province*. Doctoral Thesis. Changsha: Central South University, 1–186. (in Chinese).

Deering, C. D., and Bachmann, O. (2010). Trace Element Indicators of Crystal Accumulation in Silicic Igneous Rocks. *Earth Planet. Sci. Lett.* 297, 324–331. doi:10.1016/j.epsl.2010.06.034

Dostal, J., Kontak, D. J., Gerel, O., Gregory Shellnutt, J., and Fayek, M. (2015). Cretaceous Ongonites (Topaz-bearing Albite-Rich Microleucogranites) from Ongon Khairkhan, Central Mongolia: Products of Extreme Magmatic Fractionation and Pervasive Metasomatic Fluid: Rock Interaction. *Lithos* 236-237, 173–189. doi:10.1016/j.lithos.2015.08.003

Ferry, J. M., and Watson, E. B. (2007). New Thermodynamic Models and Revised Calibrations for the Ti-In-Zircon and Zr-In-Rutile Thermometers. *Contrib. Mineral. Pet.* 154 (4), 429–437. doi:10.1007/s00410-007-0201-0

Fidelis, I., and Siekierski, S. (1966). The Regularities in Stability Constants of Some Rare Earth Complexes. *J. Inorg. Nucl. Chem.* 28, 185–188. doi:10.1016/0022-1902(66)80243-9

Frost, B. R., Barnes, C. G., Collins, W. J., Arculus, R. J., Ellis, D. J., and Frost, C. D. (2001). A Geochemical Classification for Granitic Rocks. *J. Petrology* 42, 2033–2048. doi:10.1093/petrology/42.11.2033

Gelman, S. E., Deering, C. D., Bachmann, O., Huber, C., and Gutiérrez, F. J. (2014). Identifying the Crystal Graveyards Remaining after Large Silicic Eruptions. *Earth Planet. Sci. Lett.* 403, 299–306. doi:10.1016/j.epsl.2014.07.005

Gilder, S. A., Gill, J., and Coe, R. S. (1996). Isotopic and Paleo–Magmatic Constraints on the Mesozoic Tectonic Evolution of South China. *J. Geophys. Res.* 101 (B7), 13137–16154. doi:10.1029/96jb00662

Griffin, W. L., Pearson, N. J., Belousova, E., Jackson, S. E., van Achterbergh, E., O'Reilly, S. Y., et al. (2000). The Hf Isotope Composition of Cratonic Mantle: LAM-MC-ICPMS Analysis of Zircon Megacrysts in Kimberlites. *Geochimica Cosmochimica Acta* 64 (1), 133–147. doi:10.1016/s0016-7037(99)00343-9

Harris, N. B. W., and Inger, S. (1992). Trace Element Modelling of Pelite-Derived Granites. *Contr. Mineral. Pet.*. 110, 46–56. doi:10.1007/bf00310881

Hoskin, P. W. O., and Schaltegger, U. (2003). 2. The Composition of Zircon and Igneous and Metamorphic Petrogenesis. *Rev. Mineralogy Geochem.* 53, 27–62. doi:10.1515/9781501509322-005

Irber, W. (1999). The Lanthanide Tetrad Effect and its Correlation with K/Rb, Eu/Eu*, Sr/Eu, Y/Ho, and Zr/Hf of Evolving Peraluminous Granite Suites. *Geochimica Cosmochimica Acta* 63, 489–508. doi:10.1016/s0016-7037(99)00027-7

Jiang, Y.-H., Jiang, S.-Y., Zhao, K.-D., and Ling, H.-F. (2006). Petrogenesis of Late Jurassic Qianlishan Granites and Mafic Dykes, Southeast China: Implications for a Back-Arc Extension Setting. *Geol. Mag.* 143, 457–474. doi:10.1017/s0016756805001652

Kemp, A. I. S., Hawkesworth, C. J., Foster, G. L., Paterson, B. A., Woodhead, J. D., Hergt, J. M., et al. (2007). Magmatic and Crustal Differentiation History of Granitic Rocks from Hf-O Isotopes in Zircon. *Science* 315, 980–983. doi:10.1126/science.1136154

Keppler, H. (1993). Influence of Fluorine on the Enrichment of High Field Strength Trace Elements in Granitic Rocks. *Contr. Mineral. Pet.*. 114, 479–488. doi:10.1007/bf00321752

Kesler, S. E., Gruber, P. W., Medina, P. A., Keoleian, G. A., Everson, M. P., and Wallington, T. J. (2012). Global Lithium Resources: Relative Importance of Pegmatite, Brine and Other Deposits. *Ore Geol. Rev.* 48 (5), 55–69. doi:10.1016/j.oregeorev.2012.05.006

Lai, S. H., Chen, R. Y., Zhang, D., Di, Y. J., Gong, Y., Yuan, Y., et al. (2014). Petrogeochemical Features and Zircon LA-ICPMS U-Pb Ages of Granite in the Pantian Iron Ore Deposit, Fujian Province and Their Relationship with Mineralization. *Acta Petrol. Sin.* 030 (006), 1780–1792. (in Chinese).

Lai, S. H. (2015). *Research on Mineralization of the Xianghualing Tin Polymetallic Deposit, Hunan Province, China*. Doctoral Thesis. Beijing: China University of Geosciences Beijing, 1–151. (in Chinese).

Le Maitre, E. W. (2002). *Igneous Rocks: A Classification and Glossary of Terms*. Cambridge: Cambridge University Press, 1

Le Maitre, R. W. (1989). *A Classification of Igneous Rocks and Glossary of Terms: Recommendations of the IUGS Commission on the Systematics of Igneous Rocks*. Cambridge: Oxford Blackwell, 1

Lee, C.-T. A., and Morton, D. M. (2015). High Silica Granites: Terminal Porosity and Crystal Settling in Shallow Magma Chambers. *Earth Planet. Sci. Lett.* 409, 23–31. doi:10.1016/j.epsl.2014.10.040

Lenting, C., Geisler, T., Gerdes, A., Kooijman, E., Scherer, E. E., and Zeh, A. (2010). The Behavior of the Hf Isotope System in Radiation-Damaged Zircon during Experimental Hydrothermal Alteration. *Am. Mineralogist* 95, 1343–1348. doi:10.2138/am.2010.3521

Li, H., Wu, J.-H., Evans, N. J., Jiang, W.-C., and Zhou, Z.-K. (2018). Zircon Geochronology and Geochemistry of the Xianghualing A-type Granitic Rocks: Insights into Multi-Stage Sn-Polymetallic Mineralization in South China. *Lithos* 312-313, 1–20. doi:10.1016/j.lithos.2018.05.001

Li, X. H., Liu, Y., Yang, Y. H., Chen, F. K., Tu, X. L., and Qi, C. S. (2007). Rapid Separation of Lu-Hf and Sm-Nd from a Single Rock Dissolution and Precise Measurement of Hf-Nd Isotopic Ratios for National Rock Standards. *Acta Petrol. Sin.* 23, 221–226. (in Chinese).

Li, X.-H., Chen, Z., Liu, D., and Li, W.-X. (2003). Jurassic Gabbro-Granite-Syenite Suites from Southern Jiangxi Province, SE China: Age, Origin, and Tectonic Significance. *Int. Geol. Rev.* 45, 898–921. doi:10.2747/0020-6814.45.10.898

Li, X.-H., Liu, D., Sun, M., Li, W.-X., Liang, X.-R., and Liu, Y. (2004). Precise Sm-Nd and U-Pb Isotopic Dating of the Supergiant Shizhuyuan Polymetallic Deposit and its Host Granite, SE China. *Geol. Mag.* 141 (2), 225–231. doi:10.1017/s0016756803008823

Li, X.-H., Long, W.-G., Li, Q.-L., Liu, Y., Zheng, Y.-F., Yang, Y.-H., et al. (2010). Penglai Zircon Megacrysts: a Potential New Working Reference Material for Microbeam Determination of Hf-O Isotopes and U-Pb Age. *Geostand. Geoanalytical Res.* 34 (2), 117–134. doi:10.1111/j.1751-908x.2010.00036.x

Linnen, R. L., and Cuney, M. (2004). "Granite-related Rare-Element Deposits and Experimental Constraints on Ta-Nb-W-Sn-Zr-Hf Mineralization," in *Eare-Element Geochemistry and Mineral Deposits*. Editors R. L. Linnen and I. M. Samson (GAC Short Course Notes), 17, 45

Linnen, R. L., Van Lichtervelde, M., and Cerny, P. (2012). Granitic Pegmatites as Sources of Strategic Metals. *Elements* 8 (4), 275–280. doi:10.2113/gselements.8.4.275

London, D., Morgan, G. B., Babb, H. A., and Loomis, J. L. (1993). Behavior and Effects of Phosphorus in the System Na_2O–K_2O–Al_2O_3–SiO_2–P_2O_5–H_2O at 200 MPa(H_2O). *Contr. Mineral. Pet.*. 113 (4), 450–465. doi:10.1007/bf00698315

Ludwig, K. R. (2001). *Using Isoplot/EX, Version 2.49. A Geochronological Toolkit for Microsoft Excel*. San Francisco: Berkeley Geochronological Center Special Publication.

Mao, J. W., Chen, M. H., Yuan, S. D., and Guo, C. L. (2011). Geological Characteristics of the Qinhang (Or Shihang) Metallogenic Belt in South China and Spatial–Temporal Distribution Regularity of Mineral Deposits. *Acta Geol. Sin.* 85 (5), 636–658. (in Chinese).

Mao, J. W., Cheng, Y. B., Chen, M. H., and Pirajno, F. (2013). Major Types and Time-Space Distribution of Mesozoic Ore Deposits in South China and Their Geodynamic Settings. *Miner. Deposita* 48 (3), 267. doi:10.1007/s00126-012-0446-z

Mao, J. W., Li, X. F., Lehmann, B., Chen, W., Lan, X. M., and Wei, S. L. (2004b). ^{40}Ar-^{39}Ar Dating of Tin Ores and Related Granite in Furong Tin Orefield, Hunan Province, and its Geodynamic Significance. *Mineral. Deposits* 22 (2), 164–175. (in Chinese).

Mao, J. W., Stein, H., Du, A. D., Zhou, T. F., Mei, Y. X., Li, Y. F., et al. (2004a). Molybdenite Re-os Precise Dating for Molybdenite from Cu-Au-Mo Deposits in the Middle-Lower Reaches of Yangtze River Belt and its Implication for Mineralization. *Acta Geol. Sin.* 78 (1), 121–132. (in Chinese).

Mao, J. W., Xie, G. Q., Guo, C. L., and Chen, Y. C. (2007). Large-scale Tungsten-Tin Mineralization in the Nanling Region, South China: Metallogenic Ages and Corresponding Geodynamic Process. *Acta Petrol. Sin.* 23 (10), 2329–2338. (in Chinese).

Maruyama, S., and Send, T. (1986). Orogeny and Relative Plate Motions: Example of the Japanese Islands. *Tectonophysics* 127, 305–329. doi:10.1016/0040-1951(86)90067-3

Mo, Z. S. (1983). A Discussion on the Petrogenetic Classification of Granitic Rocks in the Nanling Region. *Geol. Bull. China* 1, 22–26. (in Chinese).

Mysen, B. O., and RyersonVirgo, F. J. D. (1981). The Structural Role of Phosphorus in Silicate Melts. *Am. Mineralogist* 66 (1-2), 106

Mysen, B. (1990). Relationships between Silicate Melt Structure and Petrologic Processes. *Earth-Science Rev.* 27 (4), 281–365. doi:10.1016/0012-8252(90)90055-z

Nandedkar, R. H., Hürlimann, N., Ulmer, P., and Müntener, O. (2016). Amphibole-melt Trace Element Partitioning of Fractionating Calc-Alkaline Magmas in the Lower Crust: an Experimental Study. *Contrib. Mineral. Pet.* 171, 71. doi:10.1007/s00410-016-1278-0

Patino Douce, A. E., and Harris, N. (1998). Experimental Constraints on Himalayan Anatexis. *J. Petrology* 39 (4), 689–710. doi:10.1093/petroj/39.4.689

Pearce, J. (1996). Sources and Settings of Granitic Rocks. *Episodes* 19, 120–125. doi:10.18814/epiiugs/1996/v19i4/005

Peng, J., Zhou, M.-F., Hu, R., Shen, N., Yuan, S., Bi, X., et al. (2006). Precise Molybdenite Re-os and Mica Ar-Ar Dating of the Mesozoic Yaogangxian Tungsten Deposit, Central Nanling District, South China. *Min. Deposita* 41, 661–669. doi:10.1007/s00126-006-0084-4

Peppard, D. F., Mason, G. W., and Lewey, S. (1969). A Tetrad Effect in the Liquid-Liquid Extraction Ordering of Lanthanides(III). *J. Inorg. Nucl. Chem.* 31, 2271–2272. doi:10.1016/0022-1902(69)90044-x

Pérez-Soba, C., and Villaseca, C. (2010). Petrogenesis of Highly Fractionated I-type Peraluminous Granites: La Pedriza Pluton (Spanish Central System). *Geol. Acta* 8, 131. doi:10.1344/105.000001527

Pirajno, F. (2013). "Effects of Metasomatism on Mineral Systems and Their Host Rocks: Alkali Metasomatism, Skarns, Greisens, Tourmalinites, Rodingites, Black-Wall Alteration and Listvenites," in *Metasomatism and the Chemical Transformation of Rock: Lecture Notes in Earth System Sciences*. Editors D. E. Harlov and H. Austrheim (Berlin: Springer Berlin Heidelberg), 203–251. doi:10.1007/978-3-642-28394-9_7

Putnis, A. (2009). 3. Mineral Replacement Reactions. *Rev. Mineral. Geochem* 70, 87–124. doi:10.1515/9781501508462-005

Qiu, R. Z., Deng, J. F., Cai, Z. Y., Zhou, S., Chang, H. L., and Du, S. H. (2002). Material Sources of Granite and Ore in Xianghualing Mult-Metal Orefield, Hunan Province. *Mineral. Deposits* 21 (S1), 1017–1020. (in Chinese).

Qiu, R. Z., Deng, J. F., Cai, Z. Y., Zhou, S., Chang, H. L., and Du, S. H. (2003). Nd Isotopic Characteristics and Genesis of Xianhualing 430 Granitic Body, Hunan Province. *Acta Petrologica Mineralogica* 22 (1), 41–46. (in Chinese).

Qiu, R. Z., and Peng, S. B. (1997). Gensis of Granitic Nb -Ta Deposit in Xianghualing Area and the Role of the Supercritical Fluid in the Process of Rock-Forming and Mineralization. *Hunan Geol.* 16 (2), 92–97. (in Chinese).

Qiu, R. Z., Zhou, S., Chang, H. L., Du, S. H., and Peng, S. B. (1998). The Evolution of Li-Bearing Micas from Xianghualing Granites and Their Ore-Prospecting Significance in Hunan. *J. Guilin Univ. Technol.* 18 (02), 145–153. (in Chinese).

Roda-Robles, E., Pesquera, A., Gil-Crespo, P., and Torres-Ruiz, J. (2012). From granite to highly evolved pegmatite: A case study of the Pinilla de Fermoselle granite-pegmatite system (Zamora, Spain). *Lithos* 153, 192–207. doi:10.1016/j.lithos.2012.04.027

Schmidt, M. W., Dardon, A., Chazot, G., and Vannucci, R. (2004). The Dependence of Nb and Ta Rutile-Melt Partitioning on Melt Composition and Nb/Ta Fractionation during Subduction Processes. *Earth Planet. Sci. Lett.* 226, 415–432. doi:10.1016/j.epsl.2004.08.010

Simmons, W. B. S., and Webber, K. L. (2008). Pegmatite Genesis: State of the Art. *ejm* 20, 421–438. doi:10.1127/0935-1221/2008/0020-1833

Stepanov, A., Mavrogenes, J., Meffre, S., and Davidson, P. (2014). The Key Role of Mica during Igneous Concentration of Tantalum. *Contributions Mineralogy Petrology* 167 (6), 1–8. doi:10.1007/s00410-014-1009-3

Stepanov, A. S., and Hermann, J. (2013). Fractionation of Nb and Ta by Biotite and Phengite: Implications for the "Missing Nb Paradox". *Geology* 41, 303–306. doi:10.1130/g33781.1

Streckeisen, A., and Le Maitre, R. W. (1979). A Chemical Approximation to the Modal QAPF Classification of the Igneous Rocks. *Neues Jahrb. für Mineralogie–Abhandlungen* 136, 169

Sun, S.-s., and McDonough, W. F. (1989). "Chemical and Isotopic Systematics of Oceanic Basalts: Implications for Mantle Composition and Processes,". Editors A. D. Saunder and M. J. Norry (London: Geological Society, London, Special Publications), 42, 313–345. doi:10.1144/gsl.sp.1989.042.01.19*Geol. Soc. Lond. Spec. Publ.*

Sylvester, P. J. (1998). Post-collisional Strongly Peraluminous Granites. *Lithos* 45, 29–44. doi:10.1016/s0024-4937(98)00024-3

Taylor, S. R., and McLennan, S. M. (1985). *The Continental Crust: Its Composition and Evolution*. Oxford: Blackwell Oxford Press, 1

Thomas, R., Davidson, P., and Schmidt, C. (2011b). Extreme Alkali Bicarbonate- and Carbonate-Rich Fluid Inclusions in Granite Pegmatite from the Precambrian Rønne Granite, Bornholm Island, Denmark. *Contributions Mineralogy Petrology* 161 (2), 314–329. doi:10.1007/s00410-010-0533-z

Thomas, R., Davidson, P., and Beurlen, H. (2011a). Tantalite-(Mn) from the Borborema Pegmatite Province, Northeastern Brazil: Conditions of Formation and Melt- and Fluid-Inclusion Constraints on Experimental Studies. *Min. Deposita* 46 (7), 749–759. doi:10.1007/s00126-011-0344-9

Trumbull, R. B., and Chaussidon, M. (1999). Chemical and Boron Isotopic Composition of Magmatic and Hydrothermal Tourmalines from the Sinceni Granite-Pegmatite System in Swaziland. *Chem. Geol.* 153, 125–137. doi:10.1016/s0009-2541(98)00155-7

Van Lichtervelde, M., Holtz, F., Dziony, W., Ludwig, T., and Meyer, H.-P. (2011). Incorporation Mechanisms of Ta and Nb in Zircon and Implications for Pegmatitic Systems. *Am. Mineralogist* 96 (7), 1079–1089. doi:10.2138/am.2011.3650

Wan, T. F., and Zhu, H. (2002). Tectonics and Environment Change of Meso-Cenozoic in China Continent and its Adjacent Areas. *Geoscience* 16 (2), 107–120. (in Chinese). doi:10.1080/12265080208422884

Wang, C., Shao, Y. J., Liu, Z. F., and Zhang, Y. (2017). The Geology and Geochemistry of the Shizitou Molybdenum Deposit, Jiangxi Province, China: Implications for the Geodynamic Setting. *Acta Geol. Sin. Engl. Ed.* 91 (S1), 233–234. doi:10.1111/1755-6724.13271

Wang, C., Shao, Y., Liu, Z., Liu, Q., and Zhang, Y. (2018). Geology and Geochemistry of the Shizitou Molybdenum Deposit, Jiangxi Province: Implications for Geodynamic Setting and Metallogenesis. *Acta Geol. Sin. - Engl. Ed.* 92 (4), 1415–1431. doi:10.1111/1755-6724.13635

Wang, G.-G., Ni, P., Zhao, K.-D., Wang, X.-L., Liu, J.-Q., Jiang, S.-Y., et al. (2012). Petrogenesis of the Middle Jurassic Yinshan Volcanic-Intrusive Complex, SE China: Implications for Tectonic Evolution and Cu-Au Mineralization. *Lithos* 150, 135–154. doi:10.1016/j.lithos.2012.05.030

Wang, Y., Fan, W., Cawood, P. A., and Li, S. (2008). Sr-Nd-Pb Isotopic Constraints on Multiple Mantle Domains for Mesozoic Mafic Rocks

beneath the South China Block Hinterland. *Lithos* 106, 297–308. doi:10.1016/j.lithos.2008.07.019

Wen, C. H., Shao, Y. J., Huang, G. F., Luo, X. Y., and Li, S. M. (2017). Geochemical Features and Mineralization of Jianfengling Rare Metal Granite in Hunan Province. *Mineral. Deposits* (04), 879–892. (in Chinese).

Whalen, J. B., Currie, K. L., and Chappell, B. W. (1987). A-Type Granites: Geochemical Characteristics, Discrimination and Petrogenesis. *Contrib. Mineral. Pet.* 95, 407–419. doi:10.1007/bf00402202

Wu, F., Liu, X., Ji, W., Wang, J., and Yang, L. (2017). Highly Fractionated Granites: Recognition and Research. *Sci. China Earth Sci.* 60, 1201–1219. doi:10.1007/s11430-016-5139-1

Xiong, X. L., Zhao, Z. H., Zhu, J. C., and Rao, B. (1999). Phase Relations in Albite Granite-H_2o-HF System and Their Petro Genetic Applications. *Geochem. J.* 33 (3), 199

Xu, L. (2012). *Multi-stages Structural Deformation and its Influence on the Metallogenesis in the East Part of the Qinzhou –Hangzhou Structural Belt*. Shandong: Ocean University of China, 1–54. (in Chinese).

Xu, Y. K. (1990). *Report of Regional Geological Survey of Hunan Provinc*. Changsha: Hunan Bureau of Geology and Mineral Resources, 90–124. (in Chinese).

Xuan, Y. C., Yuan, S. D., Yuan, Y. B., and Mi, Y. R. (2014). Zircon U-Pb Age. *Geochem. petrogenesis Jianfengling Plut. South. Hunan Prov. Mineral Deposit* 33 (06), 1379–1390. (in Chinese).

Yang, L., Wu, X., Cao, J., Hu, B., Zhang, X., Gong, Y., et al. (2018). Geochronology, Petrology, and Genesis of Two Granitic Plutons of the Xianghualing Ore Field in South Hunan Province: Constraints from Zircon U-Pb Dating, Geochemistry, and Lu-Hf Isotopic Compositions. *Minerals* 8 (5), 213. doi:10.3390/min8050213

Yang, Z., de Fourestier, J., Ding, K., and Li, H. (2013). Li-bearing ferronigerite-2N1S from Xianghualing Tin-Polymetallic orefield,Hunan Province, China. *Can. Mineral.* 51, 913–919. doi:10.3749/canmin.51.6.913

Yao, J., Hua, R., Qu, W., Qi, H., Lin, J., and Du, A. (2007). Re-Os Isotope Dating of Molybdenites in the Huangshaping Pb-Zn-W-Mo Polymetallic Deposit, Hunan Province, South China and its Geological Significance. *Sci. China Ser. D.* 50, 519–526. doi:10.1007/s11430-007-2052-y

Yuan, S. D., Liu, X. F., Wang, X. D., Wu, S. H., Yuan, Y. B., Li, X. K., et al. (2012b). Geological Characteristics and ^{40}Ar-^{39}Ar Geochronology of the Hongqiling Tin Deposit in Southern Hunan Province. *Acta Petrol. Sin.* 28 (12), 3787–3797. (in Chinese). doi:10.1007/s11783-011-0280-z

Yuan, S. D., Pang, J. T., Li, H. M., Shen, N. P., and Zhang, D. L. (2008). *A Precise U-Pb Age on Cassiterite from the Xianghualing Tin-Polyrnetallic deposit(Hunan, South China) Mineralium Deposita* 43, 375–382. doi:10.1007/s00126-007-0166-y

Yuan, S. D., Peng, J. T., Shen, N. P., Hu, R. Z., and Dai, T. M. (2007). ^{40}Ar-^{39}Ar Isotopic Dating of the Xianghualing Sn-Polymetallic Orefield in Southem Hunnan and its Geological Implications. *Acta Geol. sin.* 81 (2), 278

Yuan, S. D., Zhang, D. L., Shuang, Y., Du, A. D., and Qu, W. J. (2012a). Re-Os Dating of Molybdenite from the Xintianling Giant Tungsten-Molybdenum Deposit in Southern Hunan Province, China and its Geological Implications. *Acta Petrol. Sin.* 28 (1), 27. doi:10.1007/s11783-011-0280-z

Yuan, S., Peng, J., Hao, S., Li, H., Geng, J., and Zhang, D. (2011). *In Situ* LA-MC-ICP-MS and ID-TIMS U-Pb Geochronology of Cassiterite in the Giant Furong Tin Deposit, Hunan Province, South China: New Constraints on the Timing of Tin-Polymetallic Mineralization. *Ore Geol. Rev.* 43, 235–242. doi:10.1016/j.oregeorev.2011.08.002

Zhou, L.-G., Xia, Q.-X., Zheng, Y.-F., and Hu, Z. (2014). Polyphase Growth of Garnet in Eclogite from the Hong'an Orogen: Constraints from Garnet Zoning and Phase Equilibrium. *Lithos* 206-207, 79–99. doi:10.1016/j.lithos.2014.06.020

Zhou, X. M., Sun, T., Shen, W. Z., Shu, L. S., and Niu, Y. L. (2006). Petrogenesis of Mesozoic Granitoids and Volcanic Rocks in South China: a Response to Tectonic Evolution. *Episodes* 29, 26––33. doi:10.18814/epiiugs/2006/v29i1/004

Zhu, L. (2020). *Genesis and Rare Metal Enrichment Mechanism of High-Differentiation Granites in Jianfengling, Southern Hunan*. Master Thesis. Changsha: Central South University, 4

Conflict of Interest: The authors declare that the research was conducted in the absence of any commercial or financial relationships that could be construed as a potential conflict of interest.

Publisher's Note: All claims expressed in this article are solely those of the authors and do not necessarily represent those of their affiliated organizations, or those of the publisher, the editors and the reviewers. Any product that may be evaluated in this article, or claim that may be made by its manufacturer, is not guaranteed or endorsed by the publisher.

Copyright © 2022 Ze-Yi, Yong-Jun, Han-Tao and Cheng. This is an open-access article distributed under the terms of the Creative Commons Attribution License (CC BY). The use, distribution or reproduction in other forums is permitted, provided the original author(s) and the copyright owner(s) are credited and that the original publication in this journal is cited, in accordance with accepted academic practice. No use, distribution or reproduction is permitted which does not comply with these terms.